Effects of Slowly-Varying Meniscus Curvature on Internal Flows in the Cassie State

Simon E. Game[1], Marc Hodes[2] and Demetrios T. Papageorgiou[1]†

[1]Department of Mathematics, Imperial College London, London SW7 2AZ, UK
[2]Department of Mechanical Engineering, Tufts University, Medford, MA 02138, USA

(Received xx; revised xx; accepted xx)

The flow rate of a pressure-driven liquid through a microchannel may be enhanced by texturing its no-slip boundaries with grooves aligned with the flow. In such cases, the grooves may contain vapour and/or an inert gas and the liquid is trapped in the Cassie state, resulting in (apparent) slip. The flow rate enhancement is of benefit to different applications including the increase of throughput of a liquid in a lab-on-a-chip, and the reduction of thermal resistance associated with liquid metal cooling of microelectronics. At any given cross section, the meniscus takes the approximate shape of a circular arc whose curvature is determined by the pressure difference across it. Hence, it typically protrudes into the grooves near the inlet of a microchannel and is gradually drawn into the microchannel as it is traversed and the liquid pressure decreases. For sufficiently large Reynolds numbers, the variation of the meniscus shape and hence the flow geometry necessitates the inclusion of inertial (non-parallel) flow effects. We capture them for a slender microchannel, where our small parameter is the ratio of ridge pitch-to-microchannel height, and order one Reynolds numbers. This is done by using a hybrid analytical-numerical method to resolve the nonlinear three-dimensional (3D) problem as a sequence of two-dimensional (2D) linear ones in the microchannel cross-section, allied with nonlocal conditions that determine the slowly-varying pressure distribution at leading and first orders. When the pressure difference across the microchannel is constrained by the advancing contact angle of the liquid on the ridges and its surface tension (which are high for liquid metals), inertial effects can significantly reduce the flow rate for realistic parameter values. For example, when the solid fraction of the ridges is 0.1, the microchannel height-to-(half) ridge pitch ratio is 6, the Reynolds number of the flow is 1 and the small parameter is 0.1, they reduce the flow rate of a liquid metal (Galinstan) by about 50%. Conversely, for sufficiently large microchannel heights, they enhance it. Physical explanations of both of these phenomena are given.

1. Introduction

Mathematical models of flows of liquid in the Cassie state through microchannels patterned with longitudinal grooves containing a vacuum or vapor and/or inert gas, have been studied in detail. We briefly summarise some of them below and refer the reader to the recent review article by Lee *et al.* (2016) for further details - experimental results are also discussed there. We note that as regularly pointed out in the literature (see, for example, Lee *et al.* (2016); Peaudecerf *et al.* (2017); Song *et al.* (2018)), experimental measurements of drag reduction tend to be far below those predicted theoretically.

† Email address for correspondence: d.papageorgiou@imperial.ac.uk

Depending on the flow conditions, various (and often coupled) factors, such as gas-phase viscosity (see, e.g., Asmolov *et al.* (2018)), edge effects (see, e.g., Game *et al.* (2017)), meniscus curvature (see, e.g., Sbragaglia & Prosperetti (2007)) and thermocapillary stress (see, e.g., Hodes *et al.* (2017)), may play a role in resolving the discrepancies. A phenomenon that is lately receiving increased attention due to the studies of Peaudecerf *et al.* (2017) and Song *et al.* (2018), is the substantial or full immobilisation of menisci due to Maragoni stresses along them arising from even trace amounts of surfactants in water. In this study we identify and quantify yet another mechanism, namely inertial effects due to slowly-varying meniscus curvature, that must be considered to fully resolve the discrepancies between theory and experiment. As in the case of meniscus curvature, it can result in non-neglibible reduction or enhancement of the flow rate for a fixed pressure difference across a superhydrophobic (SH) micrcochannel at realistic operating conditions. We note that until pressure-driven flow experiments are performed with water under sufficiently pristine conditions to eliminate surfactant effects, or with a liquid (perhaps a liquid metal) in the Cassie state not subject to Marangoni stresses on account of trace amounts of surfactants, we are unable to verify our own predictions against experimental data.

In a seminal study, Philip (1972*a*,*b*) analytically resolved the fully-developed flow field and corresponding flow rate for various internal flow configurations with flat, shear-free menisci by using conformal maps to accommodate mixed boundary conditions. Lauga & Stone (2003) used Philip's analysis to find expressions for the (apparent) slip length in tubes with longitudinal grooves, and also obtained solutions for the case of transverse grooves using separation of variables. Teo & Khoo (2009) formulated and solved dual-series equations to resolve the velocity field in cases not considered by Philip, involving grooves on the upper and lower boundaries of a parallel-plate channel. Sbragaglia & Prosperetti (2007) and Teo & Khoo (2010) captured the effects of meniscus curvature asymptotically and numerically, respectively, and more recently Marshall (2017) found an exact solution for the slip length for small meniscus curvatures. Maynes *et al.* (2007) and Ng *et al.* (2010) considered the effect of gas viscosity on the flow rate, while Game *et al.* (2017) considered this effect in combination with meniscus curvature and end-wall effects.

The foregoing studies and all others pertaining to longitudinal grooves, consider two-dimensional unidirectional flows in which only a cross-section of the microchannel is considered since the flow is independent of the streamwise variable. For those studies that assume a flat meniscus, this can viewed as the limiting case where surface tension is infinite and thus the meniscus is flat throughout a microchannel. This limit tends to be invalid in practice, however, where the objective is often to maximise the flow rate of the liquid. As discussed in further detail by Game *et al.* (2018), this objective may be met by additional texturing of the longitudinal ridges to cause them to be re-entrant surfaces as originally proposed by Ahuja *et al.* (2008) and Tuteja *et al.* (2008) in the context of droplets on SHs. Then, the (metastable) contact angle between a downward-protruding meniscus and the ridges may approach 90 degrees at the entrance of a microchannel and, at its outlet it may be flat or even upward protruding. This maximises the pressure difference across a microchannel while preserving the Cassie state and thus the flow rate of the liquid. This is also relevant to the application of superhydrophobic microchannels to enhance microchannel cooling of microelectronics using a liquid metal such as Galinstan as discussed by Lam *et al.* (2015). Here lubrication is essential as the thermal resistance of the microchannel is dominated by the sensible temperature rise of the liquid metal. Meniscus curvature in this context is especially important, even when the ridges are not textured with reentrant structures, since the advancing contact angles of Galinstan

on Teflon and silicon nitride, for example, are 161.2 and 147.0 degrees, respectively (equivalently, protrusion angles of 71.2 and 57.0 degrees respectively), as reported by the measurements of Liu *et al.* (2012*a*). Notably, since Galinstan has a negligible vapour pressure at near-atmospheric conditions (see Hodes *et al.* (2014) for a summery of its thermophysical propeties) and is highly susceptible to oxidation, the space in the grooves is best kept under a high vacuum and thus the shear-free meniscus assumption, which we invoke below, is a valid one. In short, trying to maximise the flow rate of liquid through a SH microchannel, causes 3D inertial effects due to the decrease in liquid pressure along the channel. This in turn causes a gradient in meniscus curvature, thus varying the geometry of the cross-sections as a microchannel is traversed.

In the present study we make significant analytical progress by utilizing the physically-relevant limit of slow streamwise variations in the meniscus curvature that in turn imply streamwise velocity variations and the introduction of a transverse flow field. We make use of this limit to resolve 3D effects and show that they can cause significant changes to quantities of interest, such as the slip length. This limit (as applied to flow through microchannels) has been previously utilized at various points in the past, in the context of no-slip channels. We give an overview here of some significant studies that use such methodology.

As discussed by Tanner (1966), Kotorynski (1979) and Van Dyke (1983), Blasius (1910) first studied the asymptotic limit for flows through channels with slowly-varying geometry. He found expressions for the first-order perturbation of the flow field (with the channel diameter to length ratio as the small parameter) in the case of axisymmetric or two-dimensional channels. This limit was seemingly studied very little since then, until Tanner (1966) extended this analysis to find a closed form expression for the change in pressure drop (for a fixed flow rate) caused by these slow variations. Manton (1971) extended the work of Tanner (1966) to allow radial variation in the pressure gradient, and hence find a higher order expression for the pressure.

A fully 3D problem was solved by Wild *et al.* (1977) who used the slowly-varying approximation to find an exact solution for the zeroth-order velocity field and pressure for a slowly-varying channel with elliptical cross sections. Remarkably, they were also able to find the zeroth-order transverse velocity, the first-order streamwise velocity and the first-order pressure fields analytically for an order one Reynolds number. They do this for the case when the properties of the ellipse vary as a function of the streamwise dimension. They also extend this to the case in which the cross-sectional geometry is a function of the liquid pressure. Elasticity conditions are imposed on the channel boundaries in order to model blood flow through veins. The final part of this analysis is completed by fitting the relationship between cross-sectional area and pressure to experimental data. Coupling of liquid pressure with channel geometry is central to the present study, making the work of Wild *et al.* (1977) of particular interest.

General expressions for slowly-varying 3D channels were generated by Kotorynski (1979) who provided expressions for each order that can, in theory, be solved iteratively. The formulation was also applied to the particular case of a spiraling circular pipe. He also studied the case in which the channel geometry varies slowly in two dimensions.

Van Dyke (1983) studied small (as well as slow) variations in a meandering two-dimensional channel of constant width by using an intrinsic coordinate system. He found analytical expressions for the first four terms of the asymptotic expansion of the streamfunction. A 3D analogue to this problem was solved by Chadwick (1985) in the case of Stokes flow, who found that a small amount of channel curvature can actually decrease flow resistance. Following this, a survey article was written by Van Dyke (1987), covering progress made up to that point in this field of study.

The case of slowly-varying axisymmetric channels is revisited by Kotorynski (1995) who used the slowly-varying approximation to find an analytical asymptotic solution for the flow field through slowly-varying axisymmetric channels. In contrast to previous efforts, Kotorynski's solutions are valid for arbitrary radial profiles. Their formulation can, in principle, find expressions for the velocity field to any required order of accuracy.

More recently, Lauga *et al.* (2004) showed that flows through channels constrained by two parallel planes with (non-trivially) varying geometry are fully three-dimensional and discuss the implications of this with regards to mixing applications. Akbari *et al.* (2011) used a heuristic approach to relate the slowly-varying elliptic model of Wild *et al.* (1977) to that of an arbitrary cross section. They also provided comparisons to experimental data, and find good agreement, attributing this to inclusion of the inertial terms.

The previous studies exclusively examine channels with a no-slip boundary condition in which a slow geometric variation is usually imposed. There has been some work on slowly-varying channels with more exotic boundary conditions (see, e.g., Ghosal (2002)). However, the slowly-varying limit has seldom been applied to meniscus geometries in superhydrophobic microchannels. Crowdy (2017) has used this limit, in combination with an asymptotic solution to the two-dimensional problem, to capture the leading-order effect of slowly-varying meniscus geometry. This is also captured in the present study, which goes on to calculate the leading-order transverse velocity field, as well as the first-order correction to the streamwise velocity field (which arises from inertial effects).

This paper is organized as follows. We formulate our mathematical model in Section 2, and include the construction of asymptotic expansions (as part of the slowly-varying approximation) and the derivation of the resulting governing equations and boundary conditions. Our methodology for solving these equations is a hybrid of numerical and analytical methods. In Section 3 we give the analytical component of this methodology. This is subdivided into three parts, the zeroth-order streamwise velocity problem, the zeroth-order transverse velocity problem, and the first-order streamwise velocity problem. In Section 4, we outline the numerical component of our methodology. In Section 5, we give our results, primarily in terms of the flow rate perturbation due to inertia. In Section 6 we conclude with a summary.

2. Mathematical model

2.1. *Fully three-dimensional problem and boundary conditions*

We wish to calculate the volumetric flow rate of liquid flowing over parallel ridges aligned with the flow direction, including inertial effects caused by the streamwise variation in meniscus geometry. Guided by applications we assume that between the ridges there is a groove of sufficient depth to allow meniscus protrusion. We also assume that the grooves contain gas of negligible viscosity or, equivalently for our purposes, are under vacuum. We illustrate a microchannel characterized by such grooves and ridges in Fig. 1. This figure also indicates a region under consideration which, by symmetry, is representative of the entire liquid domain.

The liquid motion is governed by the steady Navier-Stokes equations and driven by a pressure drop over the microchannel length. In dimensional form the equations read,

$$\rho\left(\boldsymbol{u}\cdot\boldsymbol{\nabla}\right)\boldsymbol{u} = -\nabla p + \mu\nabla^2\boldsymbol{u}, \tag{2.1}$$

$$\nabla\cdot\boldsymbol{u} = 0, \tag{2.2}$$

where $\boldsymbol{u} = (u, v, w)$ is the velocity field in the usual Cartesian coordinate system (x, y, z) where x, y are cross-sectional coordinates and z denotes the streamwise coordinate; p

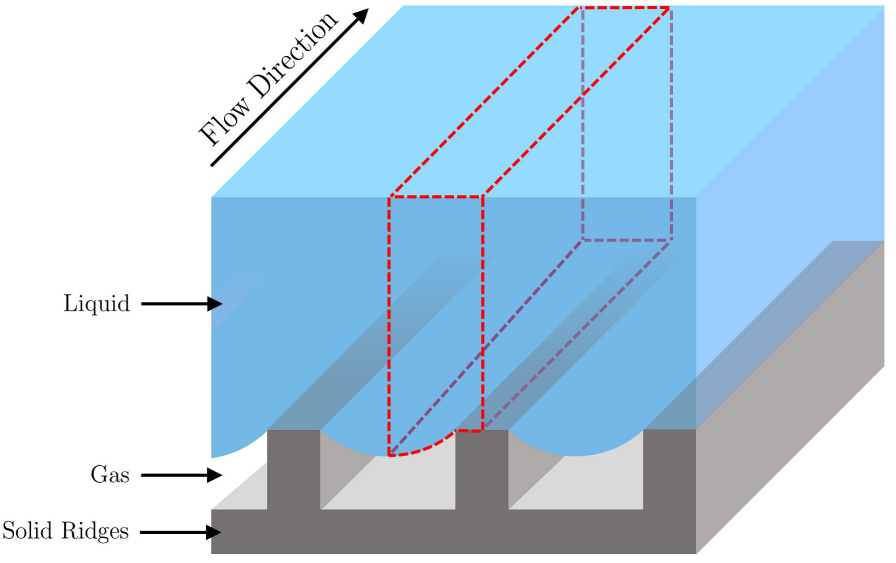


Figure 1: A section of the lower half of a superhydrophobic microchannel. The region contained within the red dotted lines represents that in which we develop our mathematical formulation. This region is illustrated in more depth in Fig. 2. The microchannel is symmetrical in the horizontal centre plane. Hence, the upper half of the microchannel (not shown) is a reflection of the lower half, in this plane.

is the pressure, ρ is the liquid density and μ its viscosity. Gravity is unimportant in the applications we are considering and is excluded. We have also assumed that the liquid is Newtonian. However, confirmation of this in the case of Galinstan has not been obtained due to complications in measuring the viscosity of liquid Gallium alloys due to formation of an elastic oxide skin (Xu *et al.* (2012)). Figure 2a illustrates the three-dimensional liquid domain, showing the distinct types of boundaries where different boundary conditions need to be applied. On the solid ridge $\boldsymbol{D}$ at $y = -H$, $\delta < x < P$, we impose a no-slip condition. On the meniscus $\boldsymbol{E}$ at the unknown interface $y = -h(x, z)$, $0 < x < \delta$, we impose zero normal velocity since we are at steady state, and a balance of normal and tangential stresses noting that the latter lead to zero shear stress conditions since the gas viscosity is negligible. At the inflow front face $\boldsymbol{A}$ of the microchannel at $z = 0$, and its back end $\boldsymbol{G}$ at $z = L$, we prescribe pressure values (when it is well-defined to do so - see below). The other boundaries $\boldsymbol{C}$, $\boldsymbol{F}$, $\boldsymbol{G}$ represent planes of symmetry, with appropriate boundary conditions imposed there. In summary, the (dimensional) boundary conditions are

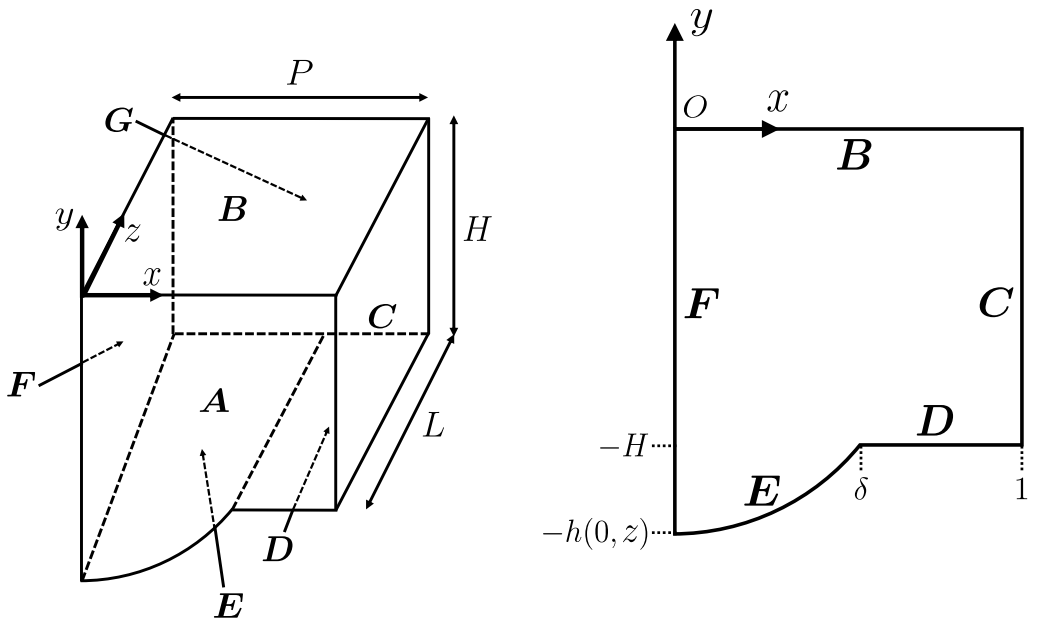


Figure 2: (a) Full 3D liquid domain and its boundaries, indicating key dimensional geometric quantities and (b) 2D cross section of the full 3D domain corresponding to an arbitrary value of z, given with corresponding boundary labels and indicating dimensionless geometric parameters. Note that the former is not drawn to scale and does not show the curvature gradient along boundary A.

$$p = p^{(1)} \qquad \text{on } \boldsymbol{A}, \tag{2.3}$$

$$\frac{\partial u}{\partial y} = v = \frac{\partial w}{\partial y} = 0 \qquad \text{on } \boldsymbol{B}, \tag{2.4}$$

$$u = \frac{\partial v}{\partial x} = \frac{\partial w}{\partial x} = 0 \qquad \text{on } \boldsymbol{C}, \tag{2.5}$$

$$\boldsymbol{u} = 0 \qquad \text{on } \boldsymbol{D}, \tag{2.6}$$

$$\boldsymbol{u} \cdot \boldsymbol{n} = 0, \qquad \boldsymbol{t}_i^T \, \boldsymbol{\sigma} \, \boldsymbol{n} = 0, \qquad \boldsymbol{n}^T \, \boldsymbol{\sigma} \, \boldsymbol{n} + p^{(0)} + \gamma\kappa = 0, \qquad \text{on } \boldsymbol{E}, \tag{2.7}$$

$$u = \frac{\partial v}{\partial x} = \frac{\partial w}{\partial x} = 0 \qquad \text{on } \boldsymbol{F}, \tag{2.8}$$

$$p = p^{(0)} \qquad \text{on } \boldsymbol{G}, \tag{2.9}$$

where κ is the mean curvature of the gas-liquid interface defined by $y = -h(x, z)$, $\boldsymbol{n}$ is an inward facing normal to this surface, $\boldsymbol{t}_i$, $i = 1, 2$ are two linearly independent vectors in a tangent plane with normal $\boldsymbol{n}$ and are chosen to be in the spanwise and streamwise directions respectively, and $\boldsymbol{\sigma} = -p\boldsymbol{I} + \mu(\boldsymbol{\nabla u} + \boldsymbol{\nabla u}^T)$ is the viscous stress tensor. Superscripts T denote the transpose of a vector.

2.2. *Nondimensionalisation and asymptotic expansions for slowly-varying microchannels*

We make analytical progress by considering the important limit when the dimensions of the microchannel cross section are much smaller than its length, i.e., $H, P \ll L$. We

nondimensionalize lengths by (half of) the ridge pitch P or microchannel length L as appropriate, and use the prescribed inlet and outlet pressures (denoted by $p^{(1)}$ and $p^{(0)}$, respectively) to re-scale the pressure as shown below. Defining $\varepsilon = P/L \ll 1$ we note that the streamwise velocity has scale $W = \varepsilon P(p^{(1)} - p^{(0)})/\mu$ and consequently the velocity in the cross-section is one order higher and scales with $U = \varepsilon W$. The following dimensionless variables are introduced (decorated with star superscripts that will be dropped later)

$$(x, y, z) = (Px^*, Py^*, Lz^*), \qquad \boldsymbol{u} = (u, v, w) = (Uu^*, Uv^*, Ww^*), \tag{2.10}$$

$$p = p^{(0)} + (p^{(1)} - p^{(0)})p^*, \quad \delta = P\delta^*, \quad H = PH^*, \quad h(x, z) = Ph^*(x^*, z^*). \tag{2.11}$$

The slowly-varying assumption is characterized by $\varepsilon \ll 1$. Substituting (2.10)-(2.11) into the Navier-Stokes and continuity equations, (2.1) and (2.2), respectively, and dropping the stars yields

$$\varepsilon^3 \mathrm{Re}(uu_x + vu_y + wu_z) = -p_x + \varepsilon^2(u_{xx} + u_{yy} + \varepsilon^2 u_{zz}), \tag{2.12a}$$

$$\varepsilon^3 \mathrm{Re}(uv_x + vv_y + wv_z) = -p_y + \varepsilon^2(v_{xx} + v_{yy} + \varepsilon^2 v_{zz}), \tag{2.12b}$$

$$\varepsilon \mathrm{Re}(uw_x + vw_y + ww_z) = -p_z + w_{xx} + w_{yy} + \varepsilon^2 w_{zz}, \tag{2.12c}$$

$$u_x + v_y + w_z = 0, \tag{2.12d}$$

where the Reynolds number $\mathrm{Re} = \rho WP/\mu$ and is assumed to be an order one quantity. We proceed with an asymptotic expansion of dependent variables in powers of ε:

$$u = u_0 + \varepsilon u_1 + ..., \quad v = v_0 + \varepsilon v_1 + ..., \quad w = w_0 + \varepsilon w_1 + ..., \tag{2.13a}$$

$$p = p_0 + \varepsilon p_1 + ..., \quad h = H + h_0 + \varepsilon h_1 + ... \tag{2.13b}$$

Substituting these expansions into the dimensionless governing equations (2.12), and the dimensionless versions of the pressure drop boundary conditions (2.3) and (2.9) gives, at leading order ε^0,

$$p_{0x} = 0, \qquad p_{0y} = 0, \qquad \nabla_\perp^2 w_0 - p_{0z} = 0, \tag{2.14a}$$

$$u_{0x} + v_{0y} = -w_{0z}, \tag{2.14b}$$

$$p_0(x, y, 0) = 1, \qquad p_0(x, y, 1) = 0. \tag{2.14c}$$

Throughout this study we use

$$\nabla_\perp^2 = \frac{\partial^2}{\partial x^2} + \frac{\partial^2}{\partial y^2}, \tag{2.15}$$

to be the Laplacian in cross-sectional variables. In section 2.3 we derive the remaining zeroth-order boundary conditions that apply at each cross section. As implied by (2.14a), the zeroth-order pressure is constant in each cross section validating our original choice of pressure drop boundary conditions. At order ε we find the system,

$$p_{1x} = 0, \qquad p_{1y} = 0, \tag{2.16a}$$

$$\nabla_\perp^2 w_1 - p_{1z} = \mathrm{Re}\,(u_0 w_{0x} + v_0 w_{0y} + w_0 w_{0z}), \tag{2.16b}$$

$$p_1(x, y, 0) = 0, \qquad p_1(x, y, 1) = 0. \tag{2.16c}$$

Note that we are interested in the $\mathcal{O}(\varepsilon)$ correction to the volumetric flow rate, and this does not require consideration of the first-order continuity equation which would only be useful in computing u_1 and v_1, which are not needed here.

At $\mathcal{O}(\varepsilon^2)$ the x and y momentum equations yield governing equations for u_0 and v_0:

$$\nabla_\perp^2 u_0 = p_{2x}, \qquad \nabla_\perp^2 v_0 = p_{2y}. \tag{2.17}$$

Solving for u_0 and v_0 is central in the analysis since they appear as forcings in the governing equation (2.16b) for w_1. Note that w_{0z} is also needed to accomplish this since it appears as a forcing in (2.14b) which is coupled to (2.17)a,b.

2.3. *Boundary Conditions*

After non-dimensionalization the zero- and first-order boundary conditions are largely identical in appearance to the boundary conditions given in (2.3)-(2.9) with the exception of the stress balances treated next. Asymptotically, these are applied at the leading-order meniscus location, $y = -H - h_0(x,z)$, with $0 < x < \delta$, and where necessary Taylor expansions are performed around this value of y to account for the higher-order terms in h. In dimensional terms, points on the liquid-gas interface are parametrized as $(x, -h(x,z), z)$, and two linearly independent unit tangent vectors $\boldsymbol{t}_1$ and $\boldsymbol{t}_2$, and the inwards pointing unit normal vector $\boldsymbol{n}$ can be expressed by:

$$\boldsymbol{t}_1 = \frac{(1,-h_x,0)^T}{\sqrt{1+h_x^2}}, \quad \boldsymbol{t}_2 = \frac{(0,-h_z,1)^T}{\sqrt{1+h_z^2}}, \quad \boldsymbol{n} = \frac{\nabla(y+h(x,z))}{|\nabla(y+h(x,z))|} = \frac{(h_x,1,h_z)^T}{\sqrt{1+h_x^2+h_z^2}}. \tag{2.18}$$

Hence the impermeability condition (2.7)a reads

$$0 = \boldsymbol{u}\cdot\boldsymbol{n} = \frac{1}{\sqrt{1+h_x^2+h_z^2}}(uh_x + v + wh_z), \tag{2.19}$$

which gives, to leading order (after non-dimensionalization and dropping stars)

$$u_0 h_{0x} + v_0 = -w_0 h_{0z}. \tag{2.20}$$

This is needed to determine the cross-flow and does not enter into the first-order analysis. The remaining conditions are the tangential and normal stress balances (2.7), namely $\boldsymbol{t}_1^T\boldsymbol{\sigma}\boldsymbol{n} = 0$, $\boldsymbol{t}_2^T\boldsymbol{\sigma}\boldsymbol{n} = 0$ and $\boldsymbol{n}^T\boldsymbol{\sigma}\boldsymbol{n} + p^{(0)} = \gamma\kappa$. We provide the detailed derivations of the zeroth- and (where necessary) first-order approximations of these boundary conditions in Appendix A, and list the results here. The condition $\boldsymbol{t}_1^T\boldsymbol{\sigma}\boldsymbol{n} = 0$, at zeroth order, gives

$$2h_{0x}(u_{0x} - v_{0y}) + (u_{0y} + v_{0x})(1 - h_{0x}^2) = h_{0z}h_{0x}w_{0y} - h_{0z}w_{0x}, \quad \text{on} \quad y = -H - h_0(x,z). \tag{2.21}$$

Once again, this condition determines the cross-flow only and is not needed to first order. The condition $\boldsymbol{t}_2^T\boldsymbol{\sigma}\boldsymbol{n} = 0$, at zeroth order, gives

$$w_{0x}h_{0x} + w_{0y} = 0, \qquad \text{on} \qquad y = -H - h_0(x,z) \tag{2.22}$$

which recovers the no-shear condition forthe two-dimensional streamwise field w_0. At first order, this tangential stress balance yields

$$w_{1x}h_{0x} + w_{1y} = h_1 w_{0yy} + h_1 w_{0xy}h_{0x} - w_{0x}h_{1x}, \qquad \text{on} \qquad y = -H - h_0(x,z). \tag{2.23}$$

The dimensionless normal stress balance (2.7)c or (A 8) fully written out, becomes at leading order,

$$p_0 = -\Gamma\frac{h_{0xx}}{(1+h_{0x}^2)^{\frac{3}{2}}}, \qquad \text{on} \qquad y = -H - h_0(x,z), \tag{2.24}$$

where $\Gamma = \gamma/(P(p^{(1)} - p^{(0)}))$. Condition (2.24) is identical to the pressure condition used in the two-dimensional parallel flow problem, and is only used to determine the coupling between the pressure and the geometry of the meniscus. As in the 2D problem, at every z, we have that $h_0(x,z)$ represents the circular arc of radius $\Gamma/p_0(z)$ with $h_{0x} = 0$ at

$x = 0$ and $h_0 = 0$ at $x = \delta$. Equivalently,

$$h_0(x,z) = \left[\left(\frac{\Gamma}{p_0(z)}\right)^2 - x^2\right]^{\frac{1}{2}} - \left[\left(\frac{\Gamma}{p_0(z)}\right)^2 - \delta^2\right]^{\frac{1}{2}}. \tag{2.25}$$

Since h_0 is determined by p_0 which is a monotonic function of z, we can instead consider it as a function of p_0 itself. Henceforth we will write $h_0(x,p_0)$ as a shorthand for $h_0(x,z(p_0))$ and likewise for other functions of z. Continuing to first order in the normal stress balance provides, on $y = -H - h_0(x,z)$,

$$p_1 = -\Gamma\left(\frac{h_{1xx}}{(1+h_{0x}^2)^{\frac{3}{2}}} - \frac{3h_{0x}h_{0xx}h_{1x}}{(1+h_{0x}^2)^{\frac{5}{2}}}\right) = -\frac{\mathrm{d}}{\mathrm{d}x}\frac{\Gamma h_{1x}}{(1+h_{0x}^2)^{\frac{3}{2}}}. \tag{2.26}$$

Recalling that p_1 is independent of x and y (see (2.16a)), and integrating (2.26) in x gives

$$xp_1 = -\frac{\Gamma h_{1x}}{(1+h_{0x}^2)^{\frac{3}{2}}}, \tag{2.27}$$

since, by symmetry, we require $h_{1x}(0) = 0$. Using (2.24) in (2.27) casts the latter into

$$h_{1x} = \frac{p_1}{p_0} x h_{0xx}. \tag{2.28}$$

Integrating by parts gives

$$h_1(x,p_0) = p_1(p_0)g_1(x,p_0), \tag{2.29}$$

where

$$g_1(x,p_0) = \frac{1}{p_0}(xh_{0x} - h_0 - \delta h_{0x}(\delta)). \tag{2.30}$$

The conditions $h_0(\delta) = h_1(\delta) = 0$ have been used to fix the integration constant. Note that g_1 is well defined. In particular, we can evaluate $g_1(x,p_0)$ at $p_0 = 0$, as revealed by an asymptotic expansion of (2.25) for small p_0 which gives

$$h_0 \sim \frac{p_0}{2\Gamma}(\delta^2 - x^2) + \mathcal{O}(p_0^3) \qquad \text{as } p_0 \to 0. \tag{2.31}$$

3. Semi-analytical solution and calculation of the volumetric flow rate

One of the central objectives of the present work is the calculation of the volumetric flow rate due to the effect of slow variations in the meniscus curvature. Recall that applications seek to maximize the pressure drop and hence the inlet meniscus curvature - the meniscus then relaxes to a flat interface at the microchannel exit assuming the pressure reaches its ambient value. We derive expressions for Q_0 and Q_1, say, the first two terms of the asymptotic expansion of the volumetric flow rate through the microchannel. As we show below, Q_0 depends on the leading-order streamwise velocity $w_0(x,y,z)$ and leading-order meniscus shape $h_0(x,z)$ which need to be determined together since the leading-order pressure gradient dp_0/dz is not known at a given cross-section - we show below how we can solve this problem. The correction Q_1 in turn depends on the streamwise velocity correction w_1, the correction p_1 to the pressure and the associated correction h_1 to the interfacial shape. To accomplish this calculation we need to solve for the cross-flow velocities and in addition need to retain inertial effects as we see below.

3.1. *Volumetric Flow Rate*

We begin by formally deriving the expansion for the volumetric flow rate in the form

$$Q = Q_0 + \varepsilon Q_1 + \dots. \tag{3.1}$$

Integrating the continuity equation (2.12)d over an interval $z_1 \leqslant z \leqslant z_2$ and applying the divergence theorem leads to

$$\int\int_{D(z_1)} w(x,y,z_1)\mathrm{d}x\mathrm{d}y = \int\int_{D(z_2)} w(x,y,z_2)\mathrm{d}x\mathrm{d}y = Q, \tag{3.2}$$

where Q is the constant flow rate (we are at steady state), $0 \leqslant z_1 < z_2 \leqslant 1$ are arbitrary and $D(z)$ is the cross section (normal to the streamwise direction) of the 3D domain at the streamwise station z. Due to the arbitrary nature of z_1 and z_2, it follows that for every $0 \leqslant z \leqslant 1$

$$\int\int_{D(z)} w(x,y,z)\mathrm{d}x\mathrm{d}y = Q. \tag{3.3}$$

Firstly note that

$$\int\int_{D(z)} w(x,y,z)\mathrm{d}x\mathrm{d}y = \int_0^\delta \underbrace{\int_{-h(x,z)}^0 w(x,y,z)\mathrm{d}y}_{I(x,\,z)}\,\mathrm{d}x + \int_\delta^1 \int_{-H}^0 w(x,y,z)\mathrm{d}y\mathrm{d}x, \tag{3.4}$$

where we have defined $I(x,z) = \int_{-h(x,z)}^0 w(x,y,z)\mathrm{d}y$ as indicated. Note also that the interface is defined to be at $y = -h(x,z) = -(H + h_0(x,z) + \varepsilon h_1(x,z) + \dots)$. In order to find the expansion for Q, we first find that for $I(x,z)$. We start by splitting the range of integration,

$$\begin{aligned} I(x,z) = \Bigg(&\int_{-H-h_0(x,z)}^0 + \int_{-H-h_0(x,z)-\varepsilon h_1(x,z)}^{-H-h_0(x,z)} \\ &+ \int_{-H-h_0(x,z)-\varepsilon h_1(x,z)-\varepsilon^2 h_2(x,z)}^{-H-h_0(x,z)-\varepsilon h_1(x,z)} + \dots \Bigg) w(x,y,z)\mathrm{d}y. \end{aligned} \tag{3.5}$$

The third integral has size $\mathcal{O}(\varepsilon^2)$ since its range is of $\mathcal{O}(\varepsilon^2)$ and the integrand is bounded; hence it is not retained in the analysis. Next, by Taylor expanding the second integrand in (3.5) about $y = -H - h_0(x,z)$ and using the asymptotic series (2.13a) for w, we obtain

$$\begin{aligned} I(x,z) = &\int_{-H-h_0(x,z)}^0 w_0(x,y,z)\mathrm{d}y + \\ &\varepsilon\left(h_1(x,z)w_0(x,-H-h_0(x,z)) + \int_{-H-h_0(x,z)}^0 w_1(x,y,z)\mathrm{d}y \right) + \mathcal{O}(\varepsilon^2). \end{aligned} \tag{3.6}$$

Furnished with (3.6), the expressions for Q_0 and Q_1 follow readily:

$$Q_0 = \int\int_{D_0(z)} w_0(x,y,z)\mathrm{d}x\mathrm{d}y, \tag{3.7}$$

$$Q_1 = p_1 \int_0^\delta g_1(x,z)w_0(x,-H-h_0(x,z),z)\mathrm{d}x + \int\int_{D_0(z)} w_1(x,y,z)\mathrm{d}x\mathrm{d}y, \tag{3.8}$$

where $D_0(z)$ is the leading-order cross-section whose only difference from $D(z)$ is that the former has a liquid-gas meniscus boundary given by the leading-order expression

$y = -H - h_0(x, z)$. To compute Q_0 and Q_1 we need to solve for the leading-order streamwise velocity, the cross-flow problem and the first-order streamwise problem. These are addressed next.

3.2. *Zeroth-Order Streamwise Velocity Problem*

As mentioned in section 2.3 we find it convenient to work with p_0 as the streamwise independent variable rather than z. In what follows we provide a method for finding $z(p_0)$, $w_0(x, y, p_0)$ and hence Q_0 from (3.7). The difficulty is that, at each cross section, the forcing $\mathrm{d}p_0/\mathrm{d}z$ is unknown and p_0 also determines its geometry. Hence, we solve a complimentary problem that allows us to apply the numerical method without knowledge of $z(p_0)$, and use the acquired numerical results to then solve the fully-coupled problem.

Note from (2.14*a*) that since p_0 is constant in each cross section, it follows that $\mathrm{d}p_0/\mathrm{d}z$ is also constant in each cross-section. This is the only forcing in equation (2.14*a*) for w_0, hence at a fixed streamwise location, w_0 is proportional to the leading-order pressure gradient. Substituting

$$w_0 = -\frac{\mathrm{d}p_0}{\mathrm{d}z} W_0, \tag{3.9}$$

into (2.14*a*) yields the following Poisson equation at each cross-section (geometrically characterized by a fixed value of p_0)

$$\nabla_\perp^2 W_0 = -1. \tag{3.10}$$

The leading-order boundary conditions to be satisfied by solutions of (3.10) are (see section 2.3 and in particular the tangential stress balance condition (2.22) at the meniscus)

$$W_{0x} h_{0x} + W_{0y} = 0 \qquad \text{on } y = -h_0(x, p_0),\ 0 < x < \delta, \tag{3.11}$$

$$W_0 = 0 \qquad \text{on } y = -H,\ \delta < x < 1, \tag{3.12}$$

$$W_{0x} = 0 \qquad \text{on } x = 0,\ 1, \tag{3.13}$$

$$W_{0y} = 0 \qquad \text{on } y = 0. \tag{3.14}$$

This can be solved numerically using the method outlined in Section 4. We define $\widetilde{Q}_0$ to be the integral of W_0 over the leading-order cross-section D_0,

$$\widetilde{Q}_0(p_0) = \int\int_{D_0(p_0)} W_0(x, y, p_0)\mathrm{d}x\mathrm{d}y. \tag{3.15}$$

This quantity can be found numerically at discrete values $p_0^{(n)}$ as defined in (4.1). Substituting the definition (3.9) into (3.15) and making use of (3.7) gives

$$-\widetilde{Q}_0(p_0)\frac{\mathrm{d}p_0}{\mathrm{d}z} = Q_0. \tag{3.16}$$

Equation (3.16) relates the auxiliary quantity $\widetilde{Q}_0$ that we can calculate at any cross-section, to the physically-relevant constant flow-rate Q_0 that we are seeking. Rearranging (3.16) and integrating both sides with respect to p_0 (first an integration between 0 and 1 to calculate Q_0 followed by an indefinite integral between 0 and p_0) gives the following expressions for Q_0 and $z(p_0)$

$$Q_0 = \int_0^1 \widetilde{Q}_0(p')\mathrm{d}p', \tag{3.17}$$

$$z(p_0) = 1 - \frac{\int_0^{p_0} \widetilde{Q}_0(p')\mathrm{d}p'}{\int_0^1 \widetilde{Q}_0(p')\mathrm{d}p'}. \tag{3.18}$$

Having calculated the values of $\widetilde{Q}_0(p_0)$ at the Chebyshev points $p_0^{(n)}$ as defined in (4.1), we compute integrals (3.17)-(3.18) in turn using Chebyshev collocation methods. We then recover $\mathrm{d}p_0/\mathrm{d}z$ from (3.16), and obtain w_0 from the definition (3.9).

3.3. *Cross-flow problem*

In order to find a u_0 and v_0 which automatically satisfy the continuity equation (2.14b) and to eliminate p_2 from (2.17), we define a modified streamfunction ψ such that:

$$u_0(x,y,z) = \psi_y(x,y,z), \qquad v_0(x,y,z) = -\psi_x(x,y,z) + \int_y^0 w_{0z}(x,y',z)\mathrm{d}y'. \tag{3.19}$$

Cross-differentiating (2.17) to eliminate p_2, and substituting (3.19) provides the following equation for ψ

$$\psi_{xxxx} + 2\psi_{xxyy} + \psi_{yyyy} = \left(\int_y^0 w_{0z}\mathrm{d}y'\right)_{xxx} + \left(\int_y^0 w_{0z}\mathrm{d}y'\right)_{xyy}. \tag{3.20}$$

The right hand side of (3.20) is identically zero as we show next. Using the leading-order streamwise momentum equation (2.14a) we have $w_{0xx} = p_{0z} - w_{0yy}$ and so

$$\left(\int_y^0 w_{0z}\mathrm{d}y'\right)_{xxx} + \left(\int_y^0 w_{0z}\mathrm{d}y'\right)_{xyy} = \int_y^0 (p_{0xzz} - w_{0xyyz})\mathrm{d}y' - w_{0xyz} = 0, \tag{3.21}$$

since $p_{0x} = 0$ from (2.14a). Hence, in order to obtain the cross-flow we need to solve a biharmonic equation in the cross-plane,

$$\nabla_\perp^4 \psi = 0. \tag{3.22}$$

This is to be solved subject to the meniscus boundary conditions (2.20) and (2.21) which in terms of ψ read

$$h_{0x}\psi_y - \psi_x = -h_{0z}w_0 - \int_{-H-h_0(x)}^0 w_{0z}\mathrm{d}y, \tag{3.23}$$

$$4h_{0x}\psi_{xy} + (\psi_{yy} - \psi_{xx})(1 - h_{0x}^2) = h_{0z}h_{0x}w_{0y} - h_{0z}w_{0x} - 2h_{0x}w_{0z} - \int_{-H-h_0(x)}^0 w_{0xz}\mathrm{d}y(1 - h_{0x}^2). \tag{3.24}$$

Substitution of (3.19) into the remaining boundary conditions for u_0 and v_0, and then integration of the resultant tangential derivative conditions to produce equivalent Dirichlet conditions (choosing $\psi = 0$ on $y = 0$ without loss of generality), gives the remaining boundary conditions for ψ. Firstly,

$$\psi_y = 0, \qquad \psi = -\int_x^1 \int_{-H}^0 w_{0z}\mathrm{d}y\mathrm{d}x \qquad \text{on } y = -H,\ x > \delta, \tag{3.25}$$

from the no-slip and impermeability conditions on the solid ridge, respectively. Secondly,

$$\psi = 0, \qquad \psi_{xx} = \int_y^0 w_{0xz}\mathrm{d}y = 0 \qquad \text{on } x = 0, 1, \tag{3.26}$$

from impermeability at the vertical planes of symmetry and the symmetry condition on v_0, respectively. Thirdly,

$$\psi = 0, \qquad \psi_{yy} = 0 \qquad \text{on } y = 0, \tag{3.27}$$

from impermeability at the horizontal plane of symmetry and the symmetry condition on u_0, respectively. It can also be shown by integrating the tangential derivative of ψ over a section of the meniscus and applying the Gradient Theorem, that (3.23) is equivalent to:

$$\psi = -\int_{\delta}^{1}\int_{-H}^{0} w_{0z}\mathrm{d}y\mathrm{d}x - \int_{x}^{\delta}\int_{-H-h_0(x)}^{0} w_{0z}\mathrm{d}y\mathrm{d}x - \int_{x}^{\delta} w_0(x,-H-h_0(x))h_{0z}\mathrm{d}x. \quad (3.28)$$

Note that, at $x = 0$, the right-hand side of (3.28) is equal to $-\mathrm{d}Q_0/\mathrm{d}z$ (by the Leibniz integral rule), which is equal to zero, since Q_0 is constant. Hence, it can be verified that the preceding boundary conditions for ψ preserve continuity around the boundary.

This system for ψ is solved at each required cross section (according to our discretization in the p_0 direction) using the method outlined in Section 4 below.

3.4. *First-Order Streamwise Velocity Problem*

We address equations (2.16*a*)-(2.16*c*) and obtain the solutions for $p_1(p_0)$, $h_1(p_0)$, w_1 and hence Q_1 from the expression (3.8). The first-order boundary conditions to be satisfied at the curved meniscus and the solid ridge, together with symmetry conditions at $x = 0, 1$ and $y = 0$, and zero conditions for the inlet and outlet perturbation pressure read:

$$w_{1x}h_{0x} + w_{1y} = p_1(g_1h_{0x}w_{0xy} + g_1w_{0yy} - g_{1x}w_{0x}) \quad \text{on } y = -H - h_0(x), \quad (3.29)$$

$$w_1 = 0 \quad \text{on } y = -H,\ x > \delta, \quad (3.30)$$

$$w_{1x} = 0 \quad \text{on } x = 0, 1, \quad (3.31)$$

$$w_{1y} = 0 \quad \text{on } y = 0, \quad (3.32)$$

$$p_1 = 0 \quad \text{on } z = 0, 1. \quad (3.33)$$

The tangential stress condition (3.29) follows from (2.23) after use of (2.29) and (2.30) for h_1. An apparent complexity in the above system is the fact that p_1 is unknown and depends on p_0 which in turn determines the geometry of the domain. This is resolved by utilizing the linearity of the problem and identifying three p_1-independent auxiliary problems whose solutions are superimposed with p_1 as a multiplicative function. The auxiliary problems need to be addressed numerically but are either similar to or identical to the solution for w_0 described in Section 3.2, so that our existing numerical algorithms can be used. Once the functional form of the solutions are found, we address the fully coupled problem as described next. To motivate the decomposition consider (2.16*b*) written in the form

$$w_{1xx} + w_{1yy} = \frac{\mathrm{d}p_1}{\mathrm{d}p_0}\, p_{0z} + \mathrm{Re}\,(u_0w_{0x} + v_0w_{0y} + w_0w_{0z}), \quad (3.34)$$

with the first term on the right hand side following by the chain rule and the fact that $p_{1x} = p_{1y} = 0$ - see (2.16*a*). Comparison of (3.34) and the boundary conditions (3.29)-(3.33) with the leading-order streamwise problem (2.14*a*) and its boundary conditions (in particular the tangential stress balance (2.22) since the other symmetry and no-slip conditions are homogeneous), shows that we must deal with three inhomogeneous terms to solve the problem. These are the right hand side of (3.29) where the only unknown is the function multiplying p_1, along with the pressure gradient and inertial terms on the right hand side of (3.34). Hence, looking for a solution of the form

$$w_1 = p_1w_A + \frac{\mathrm{d}p_1}{\mathrm{d}p_0}w_B + \mathrm{Re}\, w_C, \quad (3.35)$$

we have

$$\nabla_\perp^2 w_A = 0, \tag{3.36}$$

$$\nabla_\perp^2 w_B = \frac{\mathrm{d}p_0}{\mathrm{d}z}, \tag{3.37}$$

$$\nabla_\perp^2 w_C = u_0 w_{0x} + v_0 w_{0y} + w_0 w_{0z}, \tag{3.38}$$

subject to the boundary conditions

$$w_{Ax} h_{0x} + w_{Ay} = g_1 h_{0x} w_{0xy} + g_1 w_{0yy} - g_{1x} w_{0x}, \tag{3.39}$$

$$w_{Bx} h_{0x} + w_{By} = w_{Cx} h_{0x} + w_{Cy} = 0 \qquad \text{on } y = -H - h_0(x), \tag{3.40}$$

$$w_A = w_B = w_C = 0 \qquad \text{on } y = -H,\ x > \delta, \tag{3.41}$$

$$w_{Ax} = w_{Bx} = w_{Cx} = 0 \qquad \text{on } x = 0, 1, \tag{3.42}$$

$$w_{Ay} = w_{By} = w_{Cy} = 0 \qquad \text{on } y = 0. \tag{3.43}$$

Note that the solution w_B is identical to w_0 which so is already known - $w_B = -(\mathrm{d}p_0/\mathrm{d}z)W_0$ with W_0 already found from (3.10)-(3.14). The remaining solutions w_A and w_C can be found at each required cross section by discretization in p_0 using the methods of Section 4.

To obtain the correction Q_1 to the flux given by (3.8), we integrate the solution (3.35) over any cross-sectional area $D_0(p_0)$ as defined earlier in Section 3.1. Since p_1 is a function of p_0 alone, this integration can be easily accomplished to yield

$$Q_1 = p_1 Q_A(p_0) + \frac{\mathrm{d}p_1}{\mathrm{d}p_0} Q_B(p_0) + \mathrm{Re}\, Q_C(p_0), \tag{3.44}$$

where

$$Q_A(p_0) = \int\int_{D_0(p_0)} w_A \,\mathrm{d}x\mathrm{d}y + \int_0^\delta g_1(x) w_0(x, -H - h_0(x))\mathrm{d}x, \tag{3.45}$$

$$Q_B(p_0) = \int\int_{D_0(p_0)} w_B \,\mathrm{d}x\mathrm{d}y, \tag{3.46}$$

$$Q_C(p_0) = \int\int_{D_0(p_0)} w_C \,\mathrm{d}x\mathrm{d}y. \tag{3.47}$$

Since $w_B = w_0$, this implies that $Q_B(p_0) = Q_0 =$ constant, and so (3.44) can be rearranged to give

$$\frac{\mathrm{d}p_1}{\mathrm{d}p_0} + \frac{Q_A(p_0)}{Q_0} p_1 = \frac{Q_1}{Q_0} - \mathrm{Re}\frac{Q_C(p_0)}{Q_0}, \tag{3.48}$$

which in turn can be cast into

$$\frac{\mathrm{d}}{\mathrm{d}p_0}(p_1 \Lambda(p_0)) = \frac{\Lambda(p_0)}{Q_0}\left(Q_1 - \mathrm{Re}Q_C\right), \tag{3.49}$$

where

$$\Lambda = \exp\left(\frac{1}{Q_0}\int_0^{p_0} Q_A(p_0')\mathrm{d}p_0'\right). \tag{3.50}$$

Integrating (3.49) with respect to p_0 yields

$$p_1 = \frac{1}{Q_0 \Lambda(p_0)} \int_0^{p_0} \Lambda(p_0')\big(Q_1 - \mathrm{Re}\, Q_C(p_0')\big)\,\mathrm{d}p_0', \tag{3.51}$$

where the lower limit is chosen to satisfy the outlet pressure condition $p_1 = 0$ at $p_0 = 0$.

The inlet condition for p_1 translates into $p_1 = 0$ at $p_0 = 1$, and applying this to (3.51) provides an expression for the flux correction Q_1,

$$Q_1 = \mathrm{Re}\,\overline{Q}_C, \qquad \text{where} \qquad \overline{Q}_C = \frac{\int_0^1 \Lambda(p_0')Q_C(p_0')\mathrm{d}p_0'}{\int_0^1 \Lambda(p_0')\mathrm{d}p_0'}. \tag{3.52}$$

An expression for p_1 in terms of known computable quantities follows, namely,

$$p_1(p_0) = \frac{\mathrm{Re}}{Q_0\Lambda(p_0)} \int_0^{p_0} \Lambda(p_0')\big(\overline{Q}_C - Q_C(p_0')\big)\mathrm{d}p_0'. \tag{3.53}$$

With (3.53) available we readily obtain the correction $h_1(x, p_0)$ to the interface as given by (2.29) and (2.30). In addition, using (3.53) into expression (3.35) determines the leading-order streamwise velocity $w_1(x, y, p_0)$ where it is understood that p_0 and z are interchangeable as explained above.

We emphasize that the analysis presented here must be augmented with a series of elliptic two-dimensional cross-sectional problems solved at a discretized set of streamwise nodes. The computational work is described next, and is carried out using domain decomposition and Chebyshev methods that preserve spectral accuracy. An additional complication is the presence of stress singularities at the liquid-gas-solid triple point, and we provide details of our algorithms for treating such points analytically and maintaining spectral accuracy.

4. Numerical methods

As part of our semi-analytical study, several second and fourth order two-dimensional partial differential equations (PDEs) are solved numerically at different cross-sections along the three-dimensional microchannel and our general computational approach is described next. The 2D cross-sectional domain is decomposed into two subdomains separated by a vertical line which passes through the triple contact point, as indicated in Fig. 3. Likewise, the entire 3D domain is separated into two subdomains by the vertical plane $x = \delta$ that passes through the triple contact line.

To facilitate the implementation of spectral Chebyshev discretizations for second order problems, each subdomain with cross-section 1 and 2 as indicated in Fig. 3 is transformed to the cubes $[-1, 1]^3$. The required transformations are denoted by A and B and are detailed in Appendix B. They transform the (x, y, z) coordinates to $(\xi_{i,2}, \eta_{i,2}, p_0)$ coordinates (where i corresponds to the subdomain and the subscript 2 denotes second order problems). In each coordinate, we sample $N + 1$ Chebyshev points to create a three-dimensional grid given by

$$(\xi_{i,2}^{(l)}, \eta_{i,2}^{(m)}, p_0^{(n)}) = \left[\cos\left(\frac{l\pi}{N}\right), \cos\left(\frac{m\pi}{N}\right), \cos\left(\frac{n\pi}{N}\right)\right]. \tag{4.1}$$

To solve fourth order problems such as equation (3.22), we divide the domain as before and use transformations C and D as detailed in Appendix B transforming the (x, y) coordinates into $(\xi_{i,4}, \eta_{i,4})$, adopting the notation introduced above. Note that we do not consider the z mapping here, because it is not necessary to take z derivatives of the solution of any fourth order problems. Each subdomain (in 2D space) is therefore transformed to the square $[-\cos(\pi/N), \cos(\pi/N)] \times [-\cos(\pi/N), \cos(\pi/N)]$. Hence the boundaries of the original domains have been mapped to $\xi_{i,4}, \eta_{i,4} = \pm\cos(\pi/N)$, including the division line between subdomains. We then solve the resultant PDEs in $[-1, 1] \times [-1, 1]$, slightly extending the domain of definition of the solution function. This gives an

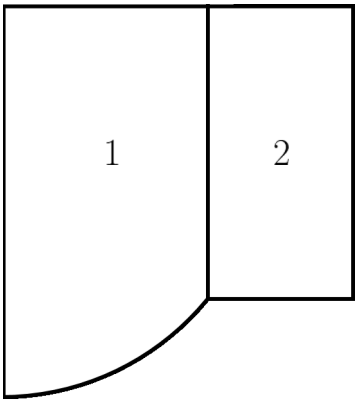


Figure 3: Diagram indicating how the cross-sectional domain is decomposed into two distinct subdomains.

extra row/column on each side of the Chebyshev grids at which the function value is not important. We use the extra degrees of freedom to impose a second boundary condition on each of the boundaries, without over-determining the discrete problem. As before, we sample $N+1$ Chebyshev points in each coordinate in $[-1,1]\times[-1,1]$ via

$$(\xi_{i,4}^{(l)},\eta_{i,4}^{(m)})=\left[\cos\left(\frac{l\pi}{N}\right),\cos\left(\frac{m\pi}{N}\right)\right]. \tag{4.2}$$

The procedure for solving the PDEs (at a fixed value of $p_0^{(n)}$) is as follows. First, we transform the governing equations and boundary conditions (including continuity between subdomains) from (x,y,z) coordinates into $(\xi_{i,j},\eta_{i,j},p_0)$ coordinates, where $j=2$ or 4. Next we express the discrete approximations to these equations at the Chebyshev grid points, using standard Chebyshev differentiation matrices - see Trefethen (2000) for example. The finite set of equations is cast into a matrix problem that was solved using MATLAB's backslash function. More details of this approach can be found in Game *et al.* (2017). Throughout this process, we remove stress singularities at the solid-liquid-gas triple point from the numerical problems, and this is found to greatly enhance the numerical convergence of the resulting problems. Such singularity removal has been discussed in the literature for superhydrophobic problems by Nizkaya *et al.* (2014), for example, and also much earlier by Peyret & Taylor (1983) in computational aspects of the Motz problem. To achieve this we require analytical asymptotic expressions for the singular parts of the solutions, and these are derived in Appendix C. The method of decomposing the solution into a singular plus a regular part is identical to that described by Game *et al.* (2018), in which the unknown strength of the singularity form is calculated as part of the numerical problem. We make a slight addition to this method where derivatives or integrals of a previously found solution are required (e.g. the compution of w_{0z}). In particular, we calculate the derivative or integral of the singular and regular parts of the solution function separately. This is due to accuracy being lost when taking, for instance, the spectral derivative of a function with infinite derivatives. In this way, we require expressions for not only the singularities, but also all of the relevant integrals and derivatives of the singularities as well. All these are also detailed in Appendix C.

Hence, after finding solutions to a PDE at each $p_0^{(n)}$, relevant quantities such as z derivatives of w_0 for example, can be calculated to be used as inhomogeneous terms for later problems (note that this typically requires polynomial interpolation between dif-

ferent coordinate systems). For this particular example we use Chebyshev differentiation matrices in the p_0 direction on the regular part of w_0 according to the transformations detailed in Appendix B. Following this, the z derivative of the singular part is calculated analytically and added to the numerical derivative of the regular part. Other quantities were calculated in a similar manner.

5. Numerical Results

5.1. *Three-dimensional flow field, pressure distribution and meniscus shape*

We initially provide a sample solution to the full problem, for the chosen parameter values of $H = 0.5$, $\Gamma = 1$ and $\delta = 0.8$ - recall that H is the dimensionless microchannel height, Γ the surface tension parameter (see (2.24) for the definition) and $1-\delta$ the size of the solid fraction. The relatively small height and small solid fraction were chosen to make the 3D effects more pronounced visually. The surface tension parameter γ was selected so that the inlet meniscus protrusion angle (in this case 53°) would be physically realisable when using a liquid metal such as Galinstan. Liu *et al.* (2012*b*) find that Galinstan has an advancing contact angle $\theta_A = 147°$ on silicon nitride, corresponding to a protrusion angle of 57°. Hence our chosen value of Γ is consistent with maintaining the Cassie state under physically relevant conditions.

In figures 4 and 5 we show the streamwise velocity profiles at zeroth and first orders, w_0 and w_1/Re, respectively, in the cross sectional region $0 < x < \delta$, $-H - h_0(x, z) < y < 0$ and $\delta < x < 1$, $-H < y < 0$, at four streamwise locations $z = 0, 1/3, 2/3$ and 1. Animated videos of these solutions (as the microchannel is traversed at a constant rate) are provided as supplementary Movie 1 for w_0 available at TOBEINSERTEDBYPUBLISHER1, and supplementary Movie 2 for w_1 available at TOBEINSERTEDBYPUBLISHER2. As can be seen from these results, the flow-field structures of w_0 and w_1 are quite similar comprising of a slow flowing region in the vicinity of the solid boundary and a faster moving central core over the meniscus and away from solid boundaries. The reason for this is the fact that the in the solution (3.35) for w_1, the main contribution comes from w_C which satisfies a Poisson equation and shares the same boundary conditions as w_0 (compare equations (3.38)-(3.39) for w_C with (3.10)-(3.11)). In addition, in contrast to w_0, w_1 is usually negative because its governing equation has $w_0 w_{0z}$ as its primary forcing, and w_{0z} is also usually positive, i.e. the leading-order flow speeds up as we move downstream. In both cases the velocity magnitudes are typically larger towards the end of the microchannel. This is a consequence of a constant flow rate being driven through a smaller channel cross section as we move downstream and the meniscus becomes flatter and explains why w_{0z} is usually positive. We provide results for large ranges of microchannel heights H later, but we emphasize that for moderate heights the trends outlined in results presented above are fairly typical in that inertia causes a slowing down of the total streamwise flow and hence a reduction in the total flux (see figure 12 and the discussion pertaining to it).

Next we consider the behaviour of the spanwise ($x-$direction) and vertical ($y-$direction) velocities, u_0 and v_0, respectively, for the transverse flow problem in the cross-section. Results are provided in figures 6 and 7, for u_0 and v_0 respectively, for the same geometry and parameters as those in figures 4 and 5. These results are captured for all streamwise locations in supplementary Movie 3 for u_0 available at TOBEINSERTEDBYPUBLISHER3, and supplementary Movie 4 for v_0 available at TOBEINSERTEDBYPUBLISHER4. Additionally, Figure 8 provides contour plots of the transverse flow field, where the colour map indicates the transverse flow speed $\sqrt{u_0^2 + v_0^2}$,

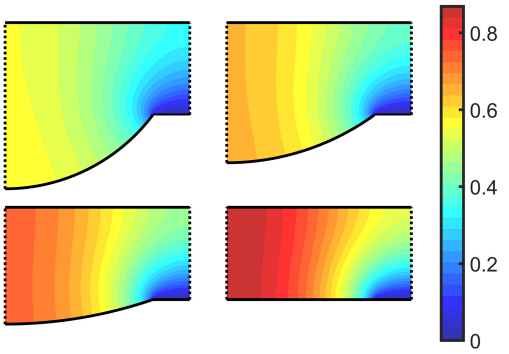


Figure 4: Contour plots of w_0 for $\Gamma = 1$, $H = 0.5$, $\delta = 0.8$, at $z = 0$, 1/3, 2/3 and 1 (from left to right).

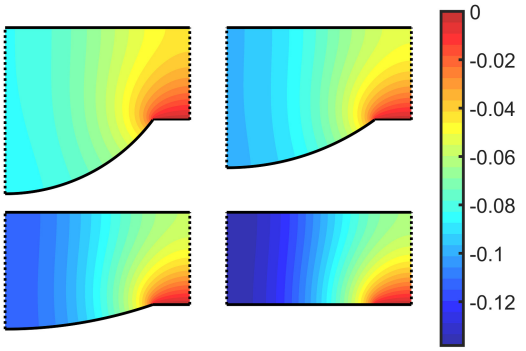


Figure 5: Contour plots of the normalised first-order correction w_1/Re to the streamwise velocity. Other parameters are $\Gamma = 1$, $H = 0.5$, $\delta = 0.8$, at $z = 0$ (top left), 1/3 (top right), 2/3 (bottom left) and 1 (bottom right).

whereas the contours indicate the transverse flow direction, that is the tangents of the contours are in the direction of the vector (u_0, v_0). Note that the contours are not streamlines in the sense that they are not lines of constant ψ as defined in equation (3.19). In all 3 figures results are, again, given at streamwise locations $z = 0$, 1/3, 2/3 and 1. It can be observed that larger transverse velocities are attained towards the end of the microchannel - for example the maximum values roughly double as we move from $z = 1/3$ to $z = 1$ as can be seen from figures 6 and 7. This increase is due to the larger values of w_0 and w_{0z} that force the system for ψ - see (3.19) for the definition of the transverse velocities in terms of the modified stream function ψ, and (3.22)-(3.23) for the equation and boundary conditions it satisfies. The results can also be used to identify where in the 3D geometry the transverse velocities attain maximum values. Inspection of figure 7 indicates that the maximum value of v_0 is achieved on the meniscus at $x = 0$ and for all streamwise values z. This is due to kinematic boundary condition (2.20). Since $h_{0x} = 0$ at $x = 0$ and $-h_{0z}$ and w_0 are at local maxima at $x = 0$, the maximum value of v_0 on the meniscus must also be here. Turning next to the streamwise velocity u_0 and the results of figure 6, it can be seen that a maximum value of u_0 is achieved close to the middle ($x \approx 0.5$) of the microchannel centerline ($y = 0$). This is largely due to transverse velocities induced at the meniscus being forced in the positive x direction

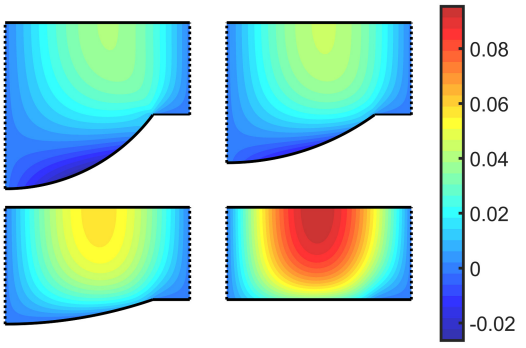


Figure 6: Contour plots of the spanwise velocity u_0 for $\Gamma = 1$, $H = 0.5$, $\delta = 0.8$, at $z = 0$ (top left) , 1/3 (top right), 2/3 (bottom left) and 1 (bottom right).

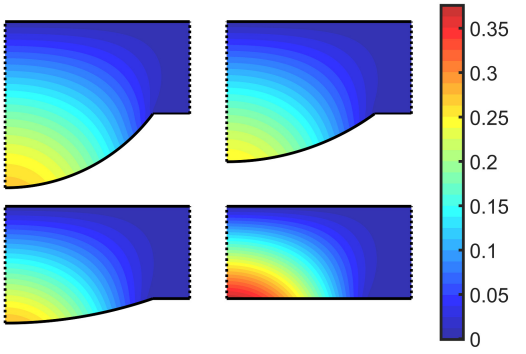


Figure 7: Contour plots of the vertical velocity v_0 for $\Gamma = 1$, $H = 0.5$, $\delta = 0.8$, at $z = 0$ (top left), 1/3 (top right), 2/3 (bottom left) and 1 (bottom right).

by the centerline and the symmetry line conditions at $x = 0$. The point in the middle of the centerline is furthest (in y) from the solid ridge that provides the source of friction , and furthest (in x) from the symmetry lines $x = 0, 1$ which force u_0 to become zero by symmetry.

Figure 9 gives the calculated pressure at zeroth and first order as a function of the streamwise position z for the parameters used earlier, namely a microchannel of height $H = 0.5$, $\delta = 0.8$ and $\Gamma = 1$. Note that since p_0 and p_1 are independent of the cross-sectional coordinates x and y dependence, they can be represented as curves of a single variable z as shown. In figure 9a, we also superimpose the dotted line $(1 - z)$ which represents a linear pressure variation for a unit pressure drop. As this figure shows, even for a case in which three-dimensional effects are inflated (small H and δ approaching 1), we see very little deviation in p_0 from the linear pressure field case. This is a result of the limited variation in the quantity $\widetilde{Q}_0$ (see equation (3.15)) along the microchannel, which itself is a result of the relatively minor influence of meniscus curvature on the 2D problem with a constant pressure gradient. We find that the deviation in p_0 is even smaller as H increases, but as discussed later in the context of figure 12b, this is the scenario when we see the largest correction in flow rate. Hence, the deflection (or lack thereof) of the zeroth order pressure field from linear is not predictive of the overall significance of three-dimensional effects. Correspondingly, figure 9b shows that the values of the

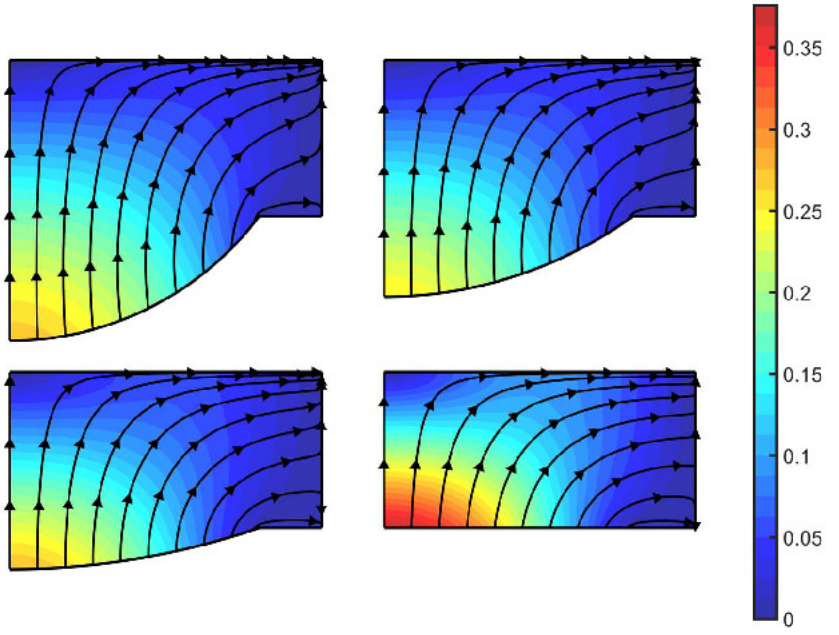
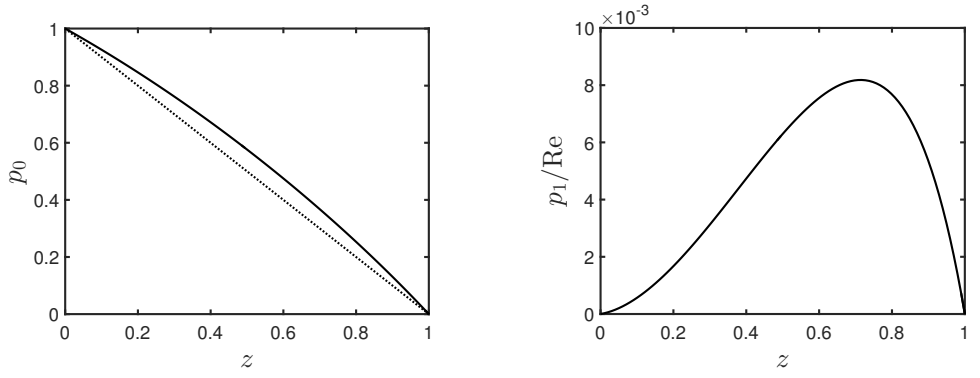


Figure 8: Contour plots illustrating the transverse flow field (u_0, v_0). The colour map indicates the transverse flow speed, $\sqrt{u_0^2 + v_0^2}$, whereas the contours indicate the transverse flow direction, i.e., tangents to the contours are in the direction of the vector (u_0, v_0). Note that the contours are not streamlines - they are not lines of constant ψ, as defined in equation (3.19). Results are depicted at streamwise locations $z = 0$ (top left), $z = 1/3$ (top right), $z = 2/3$ (bottom left) and $z = 1$ (bottom right) for $\Gamma = 1$, $H = 0.5$ and $\delta = 0.8$.

perturbation pressure p_1 we achieve for $H = 0.5$ are numerically small and of maximum magnitude $< 10^{-2}$. This does not imply small values of w_1, however. Inspection of (2.16b) (equivalently (3.34)) indicates that w_1 is driven by the first-order pressure gradient p_{1z} and the inertial terms involving leading-order velocities. The main inertial contribution comes from $w_0 w_{0z}$. The reason for this is that we find computationally that $u_0(x, y, z) \approx 0$ and $v_0(x, y, z) \approx \int_y^0 w_{0z}(x, y', z)dy'$ are excellent approximations (see equation (5.2)), and consequently even when the term $v_0 w_{0y}$ is not small relative to $w_0 w_{0z}$, its sign follows that of $w_0 w_{0z}$ (note that w_{0y} is non-negative). We conclude, therefore, that if $w_0 w_{0z}$ is positive/negative it acts like a adverse/favourable pressure-gradient thus decreasing or increasing w_1. If at the same time p_{1z} is small even though it can be adverse over more than 70% of the microchannel length as is the case in figure 9, then since w_0 is non-negative it is the sign of w_{0z} that controls whether the correction Q_1 to the flux is positive or negative. This physical reasoning helps explain our computational findings, namely for small and moderate heights H we obtain $Q_1 < 0$ and hence a reduction in the overall flow rate - fluxes are discussed in detail later, but see figure 12b for cases having



(a) (b)

Figure 9: Plots of (a) $p_0(z)$ and (b) $p_1(z)/\mathrm{Re}$ for $\Gamma = 1$, $H = 0.5$, $\delta = 0.8$. In panel (a) we also plot $(1 - z)$ against z as a dotted line to facilitate comparison with a constant pressure gradient.

$Q_1 < 0$ when $H \lessapprox 7$. It remains to explain physically the origin of positive values of $w_{0z} > 0$, the leading-order streamwise velocity gradient, generally implying an increase in w_0 along the microchannel leading to an inertia-induced reduction of the overall flow rate when H is sufficiently small. The increase in w_0 can be seen from figure 4 as we move down the microchannel, but also more explicitly in figure 13b, discussed in detail later, that shows w_{0z} at different streamwise locations for $H = 6$. As we move down the microchannel the meniscus becomes flatter and hence the cross-sectional area decreases. If we were dealing with no-slip boundaries then the conclusion that the velocity increases is immediate. In the presence of slip, however, there is a competition between the decrease in cross-sectional area and the effect of apparent slip as the meniscus flattens towards the end of the microchannel. For sufficiently small H the former mechanism dominates and the streamwise velocity increases due to cross-sectional area decrease - see also the 2D computations by Game *et al.* (2017) and the asymptotic study for small meniscus curvatures by Kirk *et al.* (2017). We also note that one can achieve significant values of p_1 at the larger values of H in the regime discussed here, as shown in figure 10 for $\delta = 0.8$ and $H = 6$ or $H = 10$. In contrast to the pressure correction p_1 corresponding to the smaller $H = 0.5$ case shown in figure 9b, we note that in addition to larger values, the pressure gradient p_{1z} is now favourable over about 0.4 units from entry before becoming adverse over the latter section of the microchannel. However, the inertial terms also see a corresponding increase in magnitude; w_{0z} decreases as H increases, but this is more than offset by the increase in w_0. Hence, the relative significance of inertia and p_1 on w_1 is left unchanged as compared to smaller H microchannels, and the overall effect is for Q_1 to remain negative for H less than 8 approximately, as seen in figure 12b. At larger H we find that Q_1 becomes positive and the physical mechanism behind this is discussed and explained later in section 5.2 where the flow-field is also interrogated in more detail.

Next we turn to the shape of the meniscus as we traverse the microchannel. As explained in section 2.2, the position of the meniscus, defined by $y = -H - h(x, z) = -H - h_0(x, z) - \epsilon h_1(x, z) + \ldots$, is found as part of the asymptotic solution procedure. The leading-order term $h_0(x, z)$ is given by the expression (2.25) which is a circular arc of changing radius $\Gamma/p_0(z)$. Hence, furnished with $p_0(z)$ computed numerically as described earlier, the leading-order shape is completely determined. In figure 11 we provide the

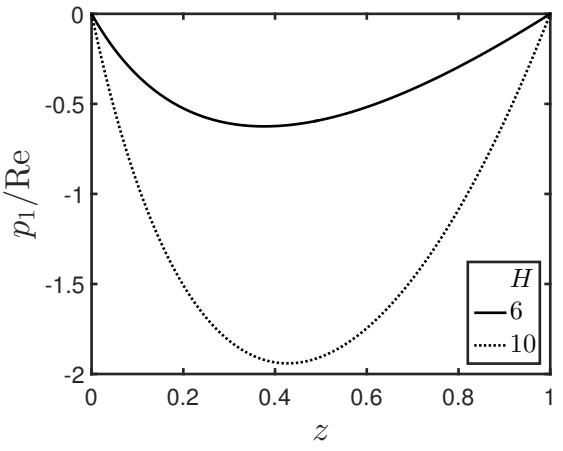


Figure 10: Plots of $p_1(z)/\mathrm{Re}$ for larger microchannel heights: $H = 6$ (solid), and $H = 10$ (dotted). Other parameters are $\Gamma = 1$, $\delta = 0.8$.

first-order correction $h_1(x, z)$ to h in order to identify any significant deviations from the leading order form - the solution for h_1 is given by equations (2.29)-(2.30). Since the meniscus shape is a quantity that varies only in the intervals $0 < x < \delta$ and $0 < z < 1$, we can display $h_1(x, z)$ as a two-dimensional contour plot as seen in figure 11. The relatively small values achieved (less than 3×10^{-3}) are a direct consequence of the relatively small values of p_1 observed in figure 9b - see solution (2.29) which tells us that h_1 depends linearly on p_1. It is of note that the perturbations to h are such that both h_0 and $h_0 + \epsilon h_1$ represent circular arcs (up to an error of $\mathrm{O}(\epsilon^2)$). This is a consequence of the application of the Young-Laplace equation with constant (in each cross section) pressure fields p_0 and $p_0 + \epsilon p_1$ respectively. Further inspection of figure 11 shows that the largest values of h_1 are in the vicinity of $x \sim 0$, i.e. the meniscus centre, which might be expected as larger values of h_0 are achieved here. The overall maximum of h_1 is seen at a streamwise location of around $z = 0.7$, which corresponds to the maximum in p_1 found in figure 9b. Physically, then, the correction h_1 will cause a local depression in the vicinity of $x \approx 0$, $z \approx 0.7$, something that could be of interest to experimentalists.

5.2. *Overall flow rates and the effects of inertia*

The results of section 5.1 provided details of the flow field, pressure distribution and meniscus shape up to two terms in the asymptotic expansion, hence yielding results correct to $\mathrm{O}(\epsilon^2)$. To illustrate matters attention was focussed on one microchannel geometry having $H = 0.5$, $\delta = 0.8$ and dimensionless surface tension $\Gamma = 1$. In this section we consider large ranges of H, δ and Γ and calculate their effect on the leading-order flow rate Q_0 and the scaled first-order correction $Q_1/(\mathrm{Re}\, Q_0)$ that introduces the effects of inertia. Recall that $Q = Q_0 + \epsilon Q_1 + \ldots$, and expressions for Q_0 and Q_1 have been derived in (3.7) (equivalently (3.17)) and (3.8) (equivalently (3.52)), respectively, and calculated using quadratures once the leading-order and first-order quantities are determined. The Reynolds number Re is included on the denominator of the quantity $Q_1/(\mathrm{Re}\, Q_0)$ because Q_1 is proportional to Re - see (3.52). We can multiply with a given value of Re to obtain the appropriate first-order flow rate as needed.

Before presenting results from the computations, we introduce two approximations to

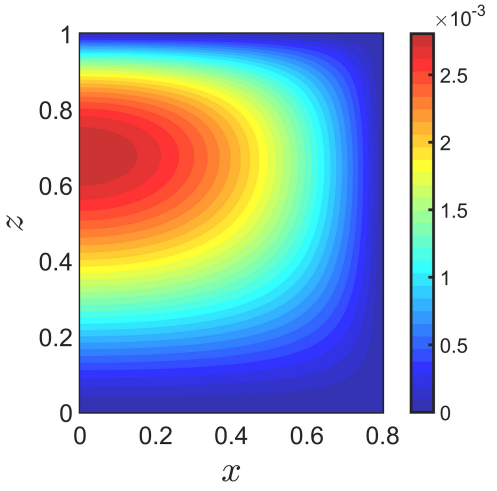


Figure 11: Contour plot of the first-order correction $h_1(x, z)$ to the meniscus shape for $\Gamma = 1$, $H = 0.5$, $\delta = 0.8$.

Q_0 and Q_1 denoted by $Q_0^{(\text{approx})}$ and $Q_1^{(\text{approx})}$, respectively. Our motivation stems from the question of whether the flow rates constructed using 3D effects (albeit for the slowly-varying case) can be approximated well using computations of 2D equations, i.e. Poisson solvers that avoid the need for computing transverse flow quantities as for example u_0 and v_0. Mathematically this simplification avoids solving biharmonic equations for the modified stream function ψ - see (3.19) and (3.22) - allied with singularity removal techniques for fourth order problems as described in Appendix C.3.

We begin with the approximation of Q_0 defined by

$$Q_0^{(\text{approx})} = \widetilde{Q}_0(p_0 = 1/2), \tag{5.1}$$

where Q_0 is given as a function of p_0 in (3.15). Instead of the exact form (3.17) for Q_0, we approximate the integrand $\widetilde{Q}_0$ by its value in the middle of the p_0-domain, i.e. at $p_0 = 1/2$, leading to the (5.1). Note that this is exactly the two-dimensional approximation that assumes a constant pressure gradient, with the meniscus protrusion angle chosen to be that corresponding to the pressure midway between inlet and outlet pressures. Next, we define $Q_1^{(\text{approx})}$ in the same way as Q_1 given by (3.8) or equivalently by (3.52), except that during the calculation process of w_C via equation (3.38) we use the following approximations for the transverse velocities u_0 and v_0

$$u_0(x, y, z) \approx u_0^{(\text{approx})}(x, y, z) = 0, \quad v_0(x, y, z) \approx v_0^{(\text{approx})}(x, y, z) = \int_y^0 w_{0z}(x, y', z)\mathrm{d}y'. \tag{5.2}$$

Specifically, to calculate w_C we substitute (5.2) for u_0 and v_0 into (3.38) and use the result to calculate Q_1 (now named $Q_1^{(\text{approx})}$) as before. We anticipate this to be a good approximation as we expect ψ to be numerically small globally (as indeed confirmed *a posteriori* from the full computations). The reason for this is that ψ, as defined by (3.19) and satisfying the biharmonic equation (3.22) and relevant boundary conditions given in section 3.3, has $\psi = 0$ imposed by boundary conditions on three sides of the domain.

We begin by presenting results for Q_0 and $Q_1/(\text{Re}Q_0)$ for a wide range of dimensionless microchannel heights H describing narrow microchannels all the way to relatively high

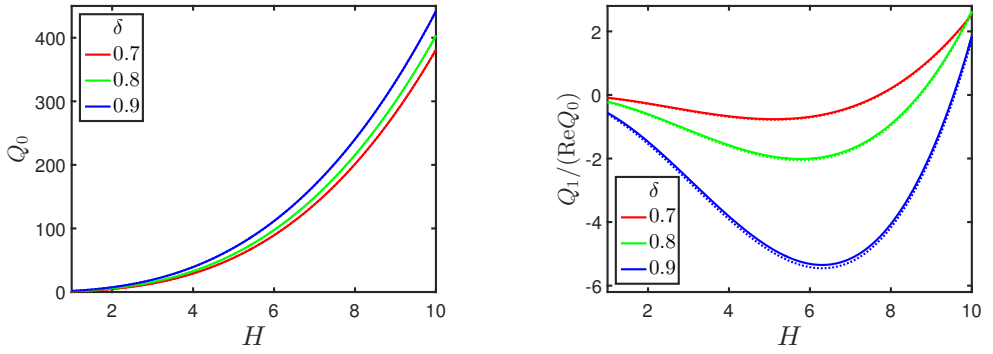
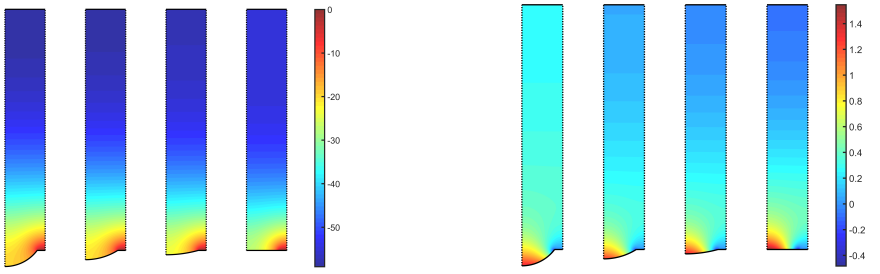


Figure 12: (a) The zeroth-order flow rate Q_0 and (b) the first-order flow rate correction metric $Q_1/(\mathrm{Re}Q_0)$ plotted against H for the indicated values of the liquid fraction δ and $\gamma = 1.2$. In both cases dotted lines represent the corresponding approximate values $Q_0^{(\mathrm{approx})}$ and $Q_1^{(\mathrm{approx})}$. Note that in both cases, but particularly in (a), the dotted lines are not easily visible due to very good agreement.

microchannels having $H = 10$. The results given in figure 12 were computed for $\delta = 0.7, 0.8, 0.9$, i.e. half-ridge lengths of 0.3, 0.2 and 0.1, respectively. The surface tension parameter is $\Gamma = 1.2$. The leading-order flow rate Q_0 is given in figure 12(a) and the correction $Q_1/(\mathrm{Re}Q_0)$ is included in panel 12(b). For each value of δ we also superimpose with dotted curves, the approximations Q_0^{approx} and Q_1^{approx} given above. The accuracy of such approximations is remarkable for the given range of H, and this finding can have practical implications for practitioners. Firstly, the success of $Q_0^{(\mathrm{approx})}$ implies that for problems where inertial effects do not need to considered, the technical details of the slowly-varying approximation results do not need to be accounted for. A practitioner can simply take the midpoint of the inlet and outlet pressures, and compute the two-dimensional problem at this pressure. Secondly, the success of $Q_1^{(\mathrm{approx})}$ indicates that the most difficult and time-consuming part of the implementation of the methodology (solving the cross-flow problem) is often unnecessary for good accuracy. In fact, the implementation of this approximation will only require the solutions to a sequence of second-order problems. It also means that significant progress may be made in finding analytical solutions, as the fourth-order problem would have been the most significant barrier to this. We expect there to be a formal way to quantify the strength of these approximations using asymptotic analysis (with H as a large parameter) as carried out in related problems, see Crowdy (2016, 2017); Kirk *et al.* (2017); Kirk (2018).

The overall trends of the results for the leading-order flow rate Q_0 shown in figure 12(a) are as expected, namely smaller width ridges produce larger flow rates due to reduced flow resistance. The results also show that this is valid for all values of H with the curve for $\delta = 0.9$ yielding the highest values and $\delta = 0.7$ the lowest ones. In addition, as expected Q_0 is monotonically increasing with H for all values of δ computed.

Figure 12b also illustrates that Q_1 is more sensitive to δ as compared to Q_0. The results also show that the behaviour of Q_1 with H is non-monotonic with a negative minimum being attained at $H \approx 6$. As explained in section 5.1, the correction Q_1 is negative for small and moderate values of H mainly due to inertial terms and in particular $w_0 w_{0z}$ being relatively large and positive compared to the other inertial terms and the correction

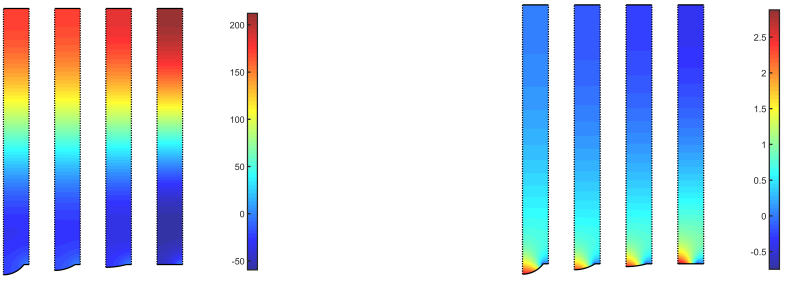


(a) (b)

Figure 13: (a) The first-order velocity w_1 and (b) the leading-order velocity gradient w_{0z}, plotted at $z = 0, 1/4, 1/2, 1$ (left to right). Other parameters are $\delta = 0.8$, $H = 6$.

p_{1z} of the pressure gradient. Figure 12b also shows that at large values of H it is possible to obtain positive values of Q_1, implying flow rate enhancement due to inertial effects. For example, Q_1 becomes positive for H larger than approximately 7.7, 8.6 or 9.5, for ridges characterized by $\delta = 0.7$, 0.8 and 0.9, respectively. A physical explanation can be given both for the sign of Q_1 in this regime as well as the requirement of larger H as δ increases and the ridge width decreases. For large H the decrease in area towards the end of the microchannel becomes insignificant compared to the enhancement in slip length due to the flattening meniscus - see Game *et al.* (2017); Kirk *et al.* (2017), for example. This slip enhancement in turn enables the leading-order flow w_0 to decrease towards the centre of the microchannel to maintain a constant flow rate. This causes w_{0z} to be negative in the centre of the microchannel away from boundaries, and hence the main inertial contribution $w_0 w_{0z}$ is negative over a large region of the cross-section and acts as a favourable pressure gradient - see equation (3.34) and the relevant discussion in section 5.1. This then causes w_1 to become positive towards the centerline and once w_1 is positive over a sufficiently large part of the microchannel, the quantity Q_1 also becomes positive. For completeness, and to quantify the physical explanation given above, we provide numerical results of the streamwise velocity correction w_1 and the key quantity w_{0z}, for a value of $\delta = 0.8$ and two values of $H = 6$ and $H = 10$ - these results correspond to the middle curve in figure 12b with $H = 6$ predicting a flow-rate decrease since $Q_1 < 0$ then, and $H = 10$ corresponding to an increase in flow-rate since $Q_1 > 0$. Results for $H = 6$ are depicted in figure 13 at the streamwise locations $z = 0, 1/4, 1/2, 1$, with w_1 and w_{0z} shown in figures 13a and 13b, respectively. The results show that w_1 is mostly negative and w_{0z} is mostly positive in the different cross-sections, explaining the negative value of Q_1 and hence the decrease in overall flow-rate. The situation is the opposite when $H = 10$ as shown in figure 14, with w_1 having large positive velocities in the majority of the microchannel driven by negative values of w_{0z}.

Finally, in Fig. 15, we provide a more complete exploration of the parameter space, giving $Q_1/(\mathrm{Re}Q_0)$ as all three parameters δ, H and Γ vary in the ranges $0.9 \leqslant \delta \leqslant 0.5$, $0.5 \leqslant H \leqslant 4$ and $2 \leqslant \Gamma \leqslant 1$. It is noteworthy that Q_1 becomes more negative for smaller Γ, as can be seen by fixing δ in any of the figures and reducing the value of Γ. This is quite intuitive since smaller Γ leads to a larger inlet meniscus curvature and therefore enhanced three-dimensional effects. Similarly, increasing δ for a fixed Γ also enhances the three-dimensional effects, which in turn causes Q_1 to become more negative.



(a) (b)

Figure 14: (a) The first-order velocity w_1 and (b) the leading-order velocity gradient w_{0z}, plotted at $z = 0, 1/4, 1/2, 1$ (left to right). Other parameters are $\delta = 0.8$, $H = 10$.

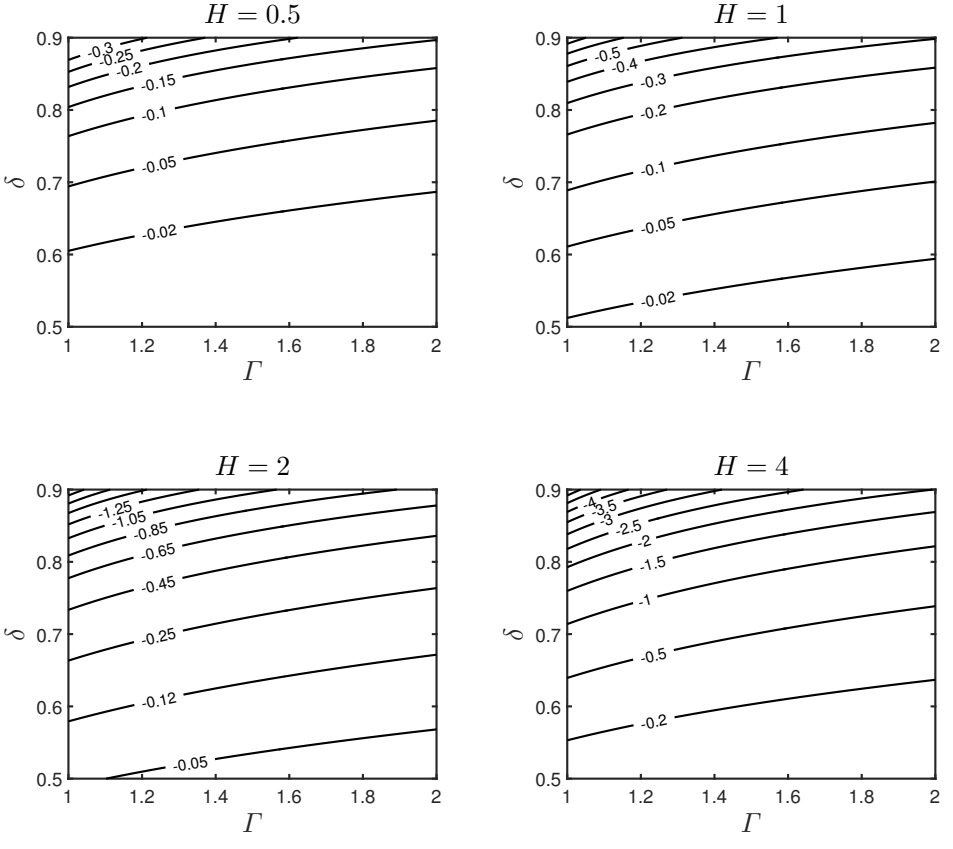


Figure 15: Contour plots of $Q_1/(\mathrm{Re}Q_0)$ against Γ and δ for the indicated values of H.

6. Conclusions

We have developed a hybrid asymptotic/numerical method to accurately compute the velocity field through a microchannel textured with periodic longitudinal grooves that support a slowly-varying meniscus protrusion and driven by a given pressure drop across the microchannel. We assume that the pressure at the microchannel outlet is the ambient one, hence the meniscus is highly curved at entry and flat at the end of the microchannel. No assumptions are made on the size of the meniscus curvature. Using the ratio of the grooves pitch to their length as a small parameter $\epsilon = P/L$, and assuming order one Reynolds numbers, we developed systematic asymptotic expansions that enable us to calculate the leading-order streamwise and transverse velocity fields along with the first-order streamwise field. Our hybrid asymptotic/numerical methodology represents a useful alternative approach to solving the full 3D Navier-Stokes equations in an evolving geometry where the liquid-gas interface that is in the Cassie state needs to be found as part of the solution by satisfying nonlinear interfacial conditions arising from stress balance laws.

The resulting flow-rate Q at steady laminar conditions is considered in detail and our asymptotic solution yields $Q = Q_0 + \epsilon Q_1 + \ldots$, where Q_0 and Q_1 are functions of the solid fraction δ, the dimensionless surface tension Γ and the dimensionless microchannel height H (non-dimensionalisation sets the pitch to unity). The first-order flow-rate Q_0 is the result of the leading-order, slowly-varying streamwise velocity and pressure, whereas the correction Q_1 has contributions due to inertia and the secondary flow in the slowly-varying microchannel cross-section. Typical computed flow fields are given for different microchannel heights ranging from small, $H = 0.5$, to large $H = 10$, and ranges of solid fractions δ and surface tension parameter Γ of practical relevance. In addition, the flow rates Q_0 and Q_1 are calculated and presented for a wide range of flow conditions. We note that while the pressure field does not deviate much from the standard linear profile, the slowly -varying geometry is of fundamental importance to the transverse flow and first-order velocity field. As expected Q_0 is always positive with larger values, for all H, as δ increases so that the ridge size gets smaller - see figure 12a. In contrast, we find that the first-order correction Q_1 is negative for small to moderate heights implying that inertial effects reduce the overall flow-rate. For microchannel heights above a critical value, H_c say, Q_1 is positive hence inducing inertia-induced enhancement of the overall flow-rate. The value of H_c depends on the solid fraction δ as well as the surface tension Γ, and for fixed Γ (as in the results of figure 12b), H_c increases as δ increases, i.e. larger heights are needed to counteract the flow-rate reduction due to inertia. The physical origin of these phenomena (discussed in detail in section 5.2) are linked to a competition between the decrease of the microchannel cross-section as the meniscus flattens towards the microchannel end, with velocity modifications there due to apparent slip effects. For small to moderate heights apparent slip is sub-dominant and area decrease effects dominate and induce an increase in the leading-order streamwise velocity w_0 (crucially w_{0z} is mostly positive towards the end of the microchannel). At large enough heights, however, the area decrease is not as important as apparent slip effects that modify w_0 so that the constant flux Q_0 can be attained with smaller maximum streamwise velocities. As a result w_{0z} is mostly negative and the inertial forcing $w_0 w_{0z}$ to the first-order streamwise velocity correction w_1, acts as a favourable pressure gradient yielding $Q_1 > 0$. Interestingly, as seen in figure 12b for instance, for given parameters δ and Γ, there is a local (and indeed global) minimum negative value of Q_1 at some H, where inertia exerts its most adverse effect on the reduction of the overall flow-rate, at least

within the context of our asymptotic analysis. It would be interesting to evaluate such findings with direct numerical simulations in the future.

Extensive computations were used to establish some highly accurate simplifying approximations in the calculation of the flow field at leading and first orders, as detailed in equations (5.1)-(5.2) and the discussion there. The accuracy of such approximations in capturing the flow-rates Q_0 and Q_1 over all ranges of parameters studied is excellent - see the results of figure 12. As seen from (5.2) such simplifications make it unnecessary to solve for the transverse flow field, rendering the entire computational problem easier since we avoid biharmonic equations such as (3.22) with stick-slip boundary conditions that require more intricate singularity removal computational techniques as outlined in Appendix C. As a consequence, the approximations can be useful to practitioners and notably for low Reynolds number problems where the flow-rate is accurately given by the approximation (5.1) requiring solution of a parallel flow problem governed by a single Poisson equation.

SG was supported by an Imperial College President's Scholarship. MH was was supported in part by NSF grant no. 1402783, and DTP was supported in part by EPSRC grant EP/L020564.

REFERENCES

Ahuja, A, Taylor, JA, Lifton, V, Sidorenko, AA, Salamon, TR, Lobaton, EJ, Kolodner, P & Krupenkin, TN 2008 Nanonails: A simple geometrical approach to electrically tunable superlyophobic surfaces. *Langmuir* **24** (1), 9–14.

Akbari, M., Sinton, D. & Bahrami, M. 2011 Viscous flow in variable cross-section microchannels of arbitrary shapes. *International Journal of Heat and Mass Transfer* **54** (17), 3970–3978.

Asmolov, Evgeny S, Nizkaya, Tatiana V & Vinogradova, Olga I 2018 Enhanced slip properties of lubricant-infused grooves. *Physical Review E* **98** (3), 033103.

Barber, R. 2002 *Elasticity*. Kluwer Academic Publishers.

Blasius, H. 1910 Laminare stromung in kanalen wechselnder breite. *Zeitschrift für Mathematik und Physik* **58**, 225–233.

Chadwick, R.S. 1985 Asymptotic analysis of stokes flow in a tortuous vessel. *Quarterly of applied mathematics* **43** (3), 325–336.

Crowdy, D.G. 2016 Analytical formulae for longitudinal slip lengths over unidirectional superhydrophobic surfaces with curved menisci. *J. Fluid Mech.* **791**, R7.

Crowdy, D.G. 2017 Effective slip length for longitudinal flow over unidirectional superhydrophobic surfaces in microchannels accounting for meniscus curvature development. *Private Communication* .

Game, S.E., Hodes, M., Keaveny, E.E. & Papageorgiou, D.T. 2017 Physical mechanisms relevant to flow resistance in textured microchannels. *Phys. Rev. Fluids* **2**, 094102.

Game, Simon, Hodes, Marc, Kirk, Toby & Papageorgiou, Demetrios T 2018 Nusselt numbers for poiseuille flow over isoflux parallel ridges for arbitrary meniscus curvature. *Journal of Heat Transfer* **140** (8), 081701.

Ghosal, S. 2002 Lubrication theory for electro-osmotic flow in a microfluidic channel of slowly varying cross-section and wall charge. *Journal of Fluid Mechanics* **459**, 103–128.

Hodes, Marc, Kirk, Toby L, Karamanis, Georgios & MacLachlan, Scott 2017 Effect of thermocapillary stress on slip length for a channel textured with parallel ridges. *Journal of Fluid Mechanics* **814**, 301–324.

Hodes, Marc, Zhang, Rui, Lam, Lisa Steigerwalt, Wilcoxon, Ross & Lower, Nate 2014 On the potential of galinstan-based minichannel and minigap cooling. *IEEE Transactions on Components, Packaging and Manufacturing Technology* **4** (1), 46–56.

Kirk, T.L. 2018 Asymptotic formulae for flow in superhydrophobic channels with longitudinal ridges and protruding menisci. *Journal of Fluid Mechanics* **839**, R3.

Kirk, T.L., Hodes, M. & Papageorgiou, D.T. 2017 Nusselt numbers for poiseuille flow over isoflux parallel ridges accounting for meniscus curvature. *Journal of Fluid Mechanics* **811**, 315–349.

Kotorynski, W.P. 1979 Slowly varying channel flows in three dimensions. *Journal of the Institute of Mathematics and Its Applications* **24**, 71–80.

Kotorynski, W.P. 1995 Viscous flow in axisymmetric pipes with slow variations. *Computers & fluids* **24** (6), 685–717.

Lam, Lisa Steigerwalt, Hodes, Marc & Enright, Ryan 2015 Analysis of galinstan-based microgap cooling enhancement using structured surfaces. *Journal of Heat Transfer* **137** (9), 091003.

Lauga, E. & Stone, H.A. 2003 Effective slip in pressure-driven stokes flow. *Journal of Fluid Mechanics* **489**, 55–77.

Lauga, E., Stroock, A.D. & Stone, H.A. 2004 Three-dimensional flows in slowly varying planar geometries. *Physics of fluids* **16** (8), 3051–3062.

Lee, Choongyeop, Choi, Chang-Hwan & Kim, Chang-Jin 2016 Superhydrophobic drag reduction in laminar flows: A critical review. *Experiments in Fluids* **57** (12), 176.

Liu, Tingyi, Sen, Prosenjit & Kim, Chang-Jin 2012*a* Characterization of nontoxic liquid-metal alloy galinstan for applications in microdevices. *Journal of Microelectromechanical Systems* **21** (2), 443–450.

Liu, T., Sen, P. & Kim, C.-J. 2012*b* Characterization of nontoxic liquid-metal alloy galinstan for applications in microdevices. *Journal of Microelectromechanical Systems* **21** (2), 443–450.

Manton, M.J. 1971 Low reynolds number flow in slowly varying axisymmetric tubes. *Journal of Fluid Mechanics* **49** (3), 451–459.

Marshall, J.S. 2017 Exact formulae for the effective slip length of a symmetric superhydrophobic channel with flat or weakly curved menisci. *SIAM Journal on Applied Mathematics* **77** (5), 1606–1630.

Maynes, D., Jeffs, K., Woolford, B. & Webb, B.W. 2007 Laminar flow in a microchannel with hydrophobic surface patterned microribs oriented parallel to the flow direction. *Physics of Fluids (1994-present)* **19** (9), 093603.

Ng, C.O., Chu, H.C.W. & Wang, C.Y. 2010 On the effects of liquid-gas interfacial shear on slip flow through a parallel-plate channel with superhydrophobic grooved walls. *Physics of Fluids (1994-present)* **22** (10), 102002.

Nizkaya, Tatiana V, Asmolov, Evgeny S & Vinogradova, Olga I 2014 Gas cushion model and hydrodynamic boundary conditions for superhydrophobic textures. *Physical Review E* **90** (4), 043017.

Peaudecerf, François J, Landel, Julien R, Goldstein, Raymond E & Luzzatto-Fegiz, Paolo 2017 Traces of surfactants can severely limit the drag reduction of superhydrophobic surfaces. *Proceedings of the National Academy of Sciences* **114** (28), 7254–7259.

Peyret, J.R. & Taylor, T.D. 1983 *Numerical methods for fluid flow*. Springer-Verlag.

Philip, J.R. 1972*a* Flows satisfying mixed no-slip and no-shear conditions. *Zeitschrift für angewandte Mathematik und Physik ZAMP* **23** (3), 353–372.

Philip, J.R. 1972*b* Integral properties of flows satisfying mixed no-slip and no-shear conditions. *Zeitschrift für angewandte Mathematik und Physik ZAMP* **23** (6), 960–968.

Sbragaglia, Mauro & Prosperetti, Andrea 2007 A note on the effective slip properties for microchannel flows with ultrahydrophobic surfaces. *Physics of Fluids* **19** (4), 043603.

Song, Dong, Song, Baowei, Hu, Haibao, Du, Xiaosong, Du, Peng, Choi, Chang-Hwan & Rothstein, Jonathan P 2018 Effect of a surface tension gradient on the slip flow along a superhydrophobic air-water interface. *Physical Review Fluids* **3** (3), 033303.

Tanner, R.I. 1966 Pressure losses in viscometric capillary tubes of slowly varying diameter. *British Journal of Applied Physics* **17** (5), 663.

Teo, C.J. & Khoo, B.C. 2009 Analysis of stokes flow in microchannels with superhydrophobic surfaces containing a periodic array of micro-grooves. *Microfluidics and nanofluidics* **7** (3), 353–382.

Teo, C.J. & Khoo, B.C. 2010 Flow past superhydrophobic surfaces containing longitudinal grooves: effects of interface curvature. *Microfluidics and Nanofluidics* **9** (2-3), 499–511.

Trefethen, L.N. 2000 *Spectral methods in MATLAB*, , vol. 10. SIAM.

Tuteja, Anish, Choi, Wonjae, Mabry, Joseph M, McKinley, Gareth H & Cohen, Robert E 2008 Robust omniphobic surfaces. *Proceedings of the National Academy of Sciences* **105** (47), 18200–18205.

Van Dyke, M. 1983 Laminar flow in a meandering channel. *SIAM Journal on Applied Mathematics* **43** (4), 696–702.

Van Dyke, M. 1987 Slow variations in continuum mechanics. *Advances in applied mechanics* **25**, 1–45.

Wild, R., Pedley, T.J. & Riley, D.S. 1977 Viscous flow in collapsible tubes of slowly varying elliptical cross-section. *J. Fluid Mech* **81** (02), 273–294.

Xu, Qin, Oudalov, Nikolai, Guo, Qiti, Jaeger, Heinrich M & Brown, Eric 2012 Effect of oxidation on the mechanical properties of liquid gallium and eutectic gallium-indium. *Physics of fluids* **24** (6), 063101.

Appendix A. Stress Conditions

Stress balances are applied at the liquid gas interface $y = -h$, which in dimensionless terms and utilizing the expansions (2.13b) reads $y = -H - h_0 - \varepsilon h_1 + \ldots$. First we calculate

$$\boldsymbol{\sigma n}^T = \frac{1}{\sqrt{1+h_x^2+h_z^2}} \begin{pmatrix} (-p+2\mu u_x)h_x + \mu(u_y+v_x) + \mu(u_z+w_x)h_z \\ \mu(u_y+v_x)h_x + (-p+2\mu v_y) + \mu(v_z+w_y)h_z \\ \mu(u_z+w_x)h_x + \mu(v_z+w_y) + (-p+2\mu w_z)h_z \end{pmatrix}. \tag{A 1}$$

The three boundary conditions we will derive are $\boldsymbol{t}_1\boldsymbol{\sigma n}^T = 0$, $\boldsymbol{t}_2\boldsymbol{\sigma n}^T = 0$ and $\boldsymbol{n\sigma n}^T + p^{(0)} = \gamma\kappa$. Using (A 1) and the expressions (2.18), the first tangential stress balance becomes

$$\mu[2u_x h_x + (u_y+v_x)(1-h_x^2) + (u_z+w_x)h_z - 2v_y h_x - (v_z+w_y)h_z h_x] = 0, \tag{A 2}$$

and in dimensionless form (using (2.10)-(2.11))

$$2u_x h_x + (u_y+v_x)(1-h_x^2) + (\varepsilon^2 u_z + w_x)h_z - 2v_y h_x - (\varepsilon^2 v_z + w_y)h_z h_x = 0. \tag{A 3}$$

The leading-order condition (2.21) follows readily.

The second zero shear stress condition $\boldsymbol{t_2\sigma n}^T = 0$ reads

$$\mu[-(u_y+v_x)h_x h_z - 2v_y h_z + (u_z+w_x)h_x + (v_z+w_y)(1-h_z^2) + 2w_z h_z] = 0, \tag{A 4}$$

and non-dimensionalizing we find

$$-\varepsilon^2(u_y+v_x)h_x h_z - 2\varepsilon^2 h_z v_y + (\varepsilon^2 u_z + w_x)h_x + (\varepsilon^2 v_z + w_y)(1-\varepsilon^2 h_z^2) + 2\varepsilon^2 h_z w_z = 0, \tag{A 5}$$

also to be evaluated at $y = -H - h_0 - \varepsilon h_1 + \ldots$. At leading and first order we find (2.22) and (2.23), respectively, the latter requiring a Taylor expansion of dependent variables about $y = -H - h_0$.

Finally, the normal stress balance condition $\boldsymbol{n\sigma n}^T + p^{(0)} + \gamma\kappa = 0$ becomes

$$\begin{aligned} &-(p^{(0)} + \gamma\kappa)(1+h_x^2+h_z^2) = -p(1+h_x^2+h_z^2) \\ &+ 2\mu\left[(u_y+v_x)h_x + u_x h_x^2 + v_y + w_z h_z^2 + (u_z+w_x)h_x h_z + (v_z+w_y)h_z\right]. \end{aligned} \tag{A 6}$$

Note also that for the surface $y = -h(x,z)$ we have

$$\kappa = -\frac{(1+h_z^2)h_{xx} - 2h_x h_z h_{xz} + (1+h_x^2)h_{zz}}{(1+h_x^2+h_z^2)^{3/2}}. \tag{A 7}$$

Non-dimensionalizing using (2.10)-(2.11) and dropping the stars yields

$$\Gamma\frac{(1+\varepsilon^2 h_z^2)h_{xx}-2\varepsilon^2 h_x h_z h_{xz}+\varepsilon^2(1+h_x^2)h_{zz}}{(1+h_x^2+\varepsilon^2 h_z^2)^{1/2}}+(1+h_x^2+\varepsilon^2 h_z^2)p$$
$$=2\varepsilon^2\left[(u_y+v_x)h_x+u_x h_x^2+v_y+\varepsilon^2 w_z h_z^2+(\varepsilon^2 u_z+w_x)h_x h_z+(\varepsilon^2 v_z+w_y)h_z\right]. \quad (A\,8)$$

It follows from (A 8) that the leading- and first-order conditions (2.24) and (2.26) are capillary pressure conditions with viscous stresses entering at higher order.

Appendix B. Coordinate transforms

Transformation A

Definition:

$$F(x,y,z)=f(\xi_{1,2},\eta_{1,2},p_0) \quad (B\,1)$$

$$x=\delta\left(\frac{\xi_{1,2}+1}{2}\right)\qquad y=(H+h_0(x))\left(\frac{\eta_{1,2}-1}{2}\right)\qquad z=z(p_0)\quad\text{is known} \quad (B\,2)$$

Derivatives:

$$\frac{\partial F}{\partial x}=\frac{2}{\delta}\left(\frac{\partial f}{\partial\xi_{1,2}}-\frac{\partial h_0}{\partial\xi_{1,2}}\frac{\eta_{1,2}-1}{H+h_0}\frac{\partial f}{\partial\eta_1}\right) \quad (B\,3)$$

$$\frac{\partial F}{\partial y}=\frac{2}{H+h_0}\frac{\partial f}{\partial\eta_{1,2}} \quad (B\,4)$$

$$\frac{\partial F}{\partial z}=\frac{\mathrm{d}p_0}{\mathrm{d}z}\frac{\partial f}{\partial p_0}-\frac{\mathrm{d}p_0}{\mathrm{d}z}\frac{\partial h_0}{\partial p_0}\frac{\eta_1-1}{H+h_0}\frac{\partial f}{\partial\eta_{1,2}} \quad (B\,5)$$

Transformation B

Definition:

$$F(x,y,z)=f(\xi_{2,2},\eta_{2,2},p_0) \quad (B\,6)$$

$$x=(1-\delta)\left(\frac{\xi_{2,2}+1}{2}\right)+\delta\qquad y=H\left(\frac{\eta_{2,2}-1}{2}\right)\qquad z=z(p_0)\quad\text{is known} \quad (B\,7)$$

Derivatives:

$$\frac{\partial F}{\partial x}=\frac{2}{1-\delta}\frac{\partial f}{\partial\xi_{2,2}} \quad (B\,8)$$

$$\frac{\partial F}{\partial y}=\frac{2}{H}\frac{\partial f}{\partial\eta_{2,2}} \quad (B\,9)$$

$$\frac{\partial F}{\partial z}=\frac{\mathrm{d}p_0}{\mathrm{d}z}\frac{\partial f}{\partial p_0} \quad (B\,10)$$

Transformation C

Definition:

$$F(x,y) = f(\xi_{1,4}, \eta_{1,4}) \tag{B 11}$$

$$x = \delta\left(\frac{\xi_{1,4} + \cos(\pi/N)}{2\cos(\pi/N)}\right) \qquad y = (H + h_0(x))\left(\frac{\eta_{1,4} - \cos(\pi/N)}{2\cos(\pi/N)}\right) \tag{B 12}$$

Derivatives:

$$\frac{\partial F}{\partial x} = \frac{2\cos(\pi/N)}{\delta}\left(\frac{\partial f}{\partial \xi_{1,4}} - \frac{\partial h_0}{\partial \xi_{1,4}}\frac{\eta_{1,4} - \cos(\pi/N)}{H + h_0}\frac{\partial f}{\partial \eta_{1,4}}\right) \tag{B 13}$$

$$\frac{\partial F}{\partial y} = \frac{2\cos(\pi/N)}{H + h_0}\frac{\partial f}{\partial \eta_{1,4}} \tag{B 14}$$

Transformation D

Definition:

$$F(x,y,z) = f(\xi_{2,4}, \eta_{2,4}) \tag{B 15}$$

$$x = (1-\delta)\left(\frac{\xi_{2,4} + \cos(\pi/N)}{2\cos(\pi/N)}\right) + \delta \qquad y = H\left(\frac{\eta_{2,4} - \cos(\pi/N)}{2\cos(\pi/N)}\right) \tag{B 16}$$

Derivatives:

$$\frac{\partial F}{\partial x} = \frac{2\cos(\pi/N)}{1-\delta}\frac{\partial f}{\partial \xi_{2,4}} \tag{B 17}$$

$$\frac{\partial F}{\partial y} = \frac{2\cos(\pi/N)}{H}\frac{\partial f}{\partial \eta_{2,4}} \tag{B 18}$$

Appendix C. Singularity Considerations

C.1. *Streamwise Velocity Problem*

The solution to the zeroth order streamwise problem $w_0(x,y)$ was fed into the next part of the overall problem, the zeroth order cross-flow problem. Likewise, the solution to this problem was fed into the subsequent part of the overall problem, the first-order streamwise problem. At each stage, transferring the previous numerically calculated solution introduces the potential for numerical errors to compound, severely impeding the convergence to the full solution. Consequently, we used a singularity removal method at each stage, which dramatically enhanced convergence and accuracy of the overall problem.

In particular, since the next part is a fourth order PDE, we used slightly different Chebyshev grids and Chebyshev interpolation on w_0. We also computed derivatives and indefinite integrals of w_0 using Chebyshev collocation methods. Since all of these Chebyshev methods rely on acting upon globally well-behaved functions, handled the regular and singular parts of w_0 separately. Hence, all of the required work was done

analytically on the singular part, f, and numerically on the regular part, $\hat{w}$. Denoting the strength of the singular part f as α, the solution was decomposed as

$$w_0(x,y,z) = \widehat{w}(x,y,z) + \alpha f(x,y,z). \tag{C 1}$$

As demonstrated by Game *et al.* (2018), the singular part f can be calculated in polar coordinates (r,φ), where r, φ are the usual radial and angular coordinates, respectively, with the ridge at $\varphi = 0$, We find

$$f(x,y,z) = r^{\lambda(z)}\sin(\lambda(z)\varphi), \tag{C 2}$$

$$\lambda(z) = \frac{(2k+1)\pi}{2(\pi+\theta(z))}, \quad \theta(z) = \arcsin(\delta p_0(z)/\Gamma), \tag{C 3}$$

$$r(x,y) = \sqrt{(x-\delta)^2+(y+H)^2}, \quad \varphi(x,y) = \begin{cases} \tan^{-1}\left(\frac{y+H}{x-\delta}\right) & y \geqslant -H \\ \tan^{-1}\left(\frac{y+H}{x-\delta}\right) + 2\pi & y < -H. \end{cases} \tag{C 4}$$

The quantity $\theta(z)$ above is the (downwards-facing) protrusion angle of the meniscus at a streamwise distance z along the microchannel. In our numerical implementation, we removed the first two singularities, i.e., $k = 0$ and $k = 1$. Note that the singular part of functions w_A and w_C also take this form, therefore, in computing these we subtract the same singular function f.

C.2. *Transferring w_0 to the cross-flow problem*

The cross-flow problem requires knowledge of the leading-order streamwise velocity w_0, its derivatives and certain indefinite integrals (in y). In order to handle the singular part f analytically, it is necessary to derive expressions for the corresponding derivatives and integrals of f. Firstly, we provide expressions for the x and y derivatives of f as defined in (C 2):

$$f_x = f_r r_x + f_\varphi \varphi_x = \cos\varphi f_r - \frac{1}{r}\sin\varphi f_\varphi = \lambda r^{\lambda-1}\sin((\lambda-1)\varphi), \tag{C 5}$$

$$f_y = f_r r_y + f_\varphi \varphi_y = \sin\varphi f_r + \frac{1}{r}\cos\varphi f_\varphi = \lambda r^{\lambda-1}\cos((\lambda-1)\varphi). \tag{C 6}$$

We also need to compute z derivatives. This is done using the chain rule, hence a useful expression to record is

$$\lambda_z = \lambda_\theta \theta_{p_0} p_{0z} = -\frac{\lambda}{\pi+\theta}\frac{\delta}{\sqrt{\gamma^2-\delta^2 p_0^2}} p_{0z}, \tag{C 7}$$

which is used in the evaluation of

$$f_z = f_\lambda \lambda_z = \lambda_z r^\lambda(\log(r)\sin(\lambda\varphi) + \varphi\cos(\lambda\varphi)). \tag{C 8}$$

It is also necessary to evaluate $\int_y^0 w_{0z}\mathrm{d}y'$ and hence it is useful to evaluate

$$\int_y^0 f_z \mathrm{d}y' = \left[\int_y^0 f \mathrm{d}y'\right]_z. \tag{C 9}$$

Prior to differentiating the integral on the right hand side of (C 9), we evaluate it at fixed values of $x \neq 0$ and z

$$\int_y^0 r^\lambda \sin(\lambda\varphi)\mathrm{d}y' = \int_{\varphi^-}^{\varphi^+}\left(\frac{x-\delta}{\cos\varphi'}\right)^\lambda \sin(\lambda\varphi')\frac{\mathrm{d}y}{\mathrm{d}\varphi'}\mathrm{d}\varphi', \tag{C 10}$$

where $\varphi^+ = \varphi(x,0)$ and $\varphi^- = \varphi(x,y)$. Since $y + H = (x-\delta)\tan\varphi$, where x is now considered constant, we can change variables to φ so that the integral in (C 10) becomes

$$(x-\delta)^{\lambda+1}\int_{\varphi^-}^{\varphi^+}\frac{\sin(\lambda\varphi')}{(\cos\varphi')^{\lambda+2}}\mathrm{d}\varphi', \tag{C 11}$$

and evaluated to yield

$$-\frac{(x-\delta)^{\lambda+1}}{\lambda+1}\left[\frac{\cos((\lambda+1)\varphi')}{(\cos\varphi')^{\lambda+1}}\right]_{\varphi^-}^{\varphi^+} = -\frac{1}{\lambda+1}[r^{\lambda+1}\cos((\lambda+1)\varphi)]_y^0. \tag{C 12}$$

Hence we can derive a complete expression for $\int_y^0 f_z \mathrm{d}y'$, namely

$$\int_y^0 f_z\mathrm{d}y' = -\frac{\lambda_z}{(\lambda+1)^2}[r^{\lambda+1}\{(\lambda{+}1)\log(r)\cos(\lambda+1)\varphi - \varphi(\lambda{+}1)\sin(\lambda+1)\varphi - \cos(\lambda+1)\varphi\}]_y^0. \tag{C 13}$$

C.3. *Singularities for ψ*

It can be shown (by coordinate transformation to polar coordinates and local analysis) that the system to be solved by the singular part of ψ, which we denote by $g(x,y,z)$, is

$$\nabla_\perp^4 g = 0, \tag{C 14}$$

subject to

$$g = 0, \tag{C 15}$$
$$g_{\varphi\varphi} = 0 \qquad \text{on } \varphi = \theta + \pi, \tag{C 16}$$
$$g = 0, \tag{C 17}$$
$$g_\varphi = 0 \qquad \text{on } \varphi = 0. \tag{C 18}$$

The following expression for g (for a fixed power, λ, of r) can be verified using the Michell solution from elasticity Barber (2002),

$$g = r^\lambda(A\cos(\lambda\varphi) + B\cos((\lambda-2)\varphi) + C\sin(\lambda\varphi) + D\sin((\lambda-2)\varphi)). \tag{C 19}$$

Since the problem is homogeneous and we require non-trivial solutions, it follows that all of the constants A, B, C, D scale together and we can assume $A = 1$ without loss of generality. Then, (C 17) implies that $B = -1$, equation (C 18) implies that

$$C = \frac{2-\lambda}{\lambda}D, \tag{C 20}$$

and (C 15) implies

$$D = -\lambda\frac{\cos(\lambda(\theta+\pi)) - \cos((\theta+\pi)(\lambda-2))}{\lambda\sin((\theta+\pi)(\lambda-2)) - (\lambda-2)\sin(\lambda(\theta+\pi))}. \tag{C 21}$$

Finally, applying (C 16) gives the following implicit expression for λ

$$\sin(2\pi\lambda - 2\theta + 2\lambda\theta) = (\lambda-1)\sin(2\theta), \tag{C 22}$$

which can be solved by standard root-finding methods. The corresponding expression for g then follows from (C 19). Note that (C 22) can have multiple solutions for λ. We take the smallest non-integer solution greater than 1 (we expect velocities to be finite), and remove the corresponding singularity.